AGU PUBLICATIONS

JGR

Journal of Geophysical Research: Solid Earth

RESEARCH ARTICLE
10.1002/2015JB012508

**Key Points:**
- Stress-driven, time-dependent afterslip can be successfully simulated by a narrow weak shear zone
- The upper mantle rheology can be determined through viscoelastic postseismic GPS observations
- Higher-order deformation heterogeneity may be explained by higher-order rheology heterogeneity

**Correspondence to:**
Y. Hu,
yhu@seismo.berkeley.edu

**Citation:**
Hu, Y., R. Bürgmann, N. Uchida, P. Banerjee, and J. T. Freymueller (2016), Stress-driven relaxation of heterogeneous upper mantle and time-dependent afterslip following the 2011 Tohoku earthquake, *J. Geophys. Res. Solid Earth*, *121*, doi:10.1002/2015JB012508.

Received 8 SEP 2015
Accepted 6 DEC 2015
Accepted article online 12 DEC 2015



# Stress-driven relaxation of heterogeneous upper mantle and time-dependent afterslip following the 2011 Tohoku earthquake

**Yan Hu[1], Roland Bürgmann[1], Naoki Uchida[2], Paramesh Banerjee[3], and Jeffrey T. Freymueller[4]**

[1]Berkeley Seismological Laboratory and Department of Earth & Planetary Science, University of California, Berkeley, California, United States, [2]Graduate School of Science, Tohoku University, Sendai, Japan, [3]Earth Observatory of Singapore, Nanyang Technological University, Singapore, [4]Geophysical Institute, University of Alaska Fairbanks, Fairbanks, Alaska, United States

**Abstract** Understanding of postseismic deformation following great subduction zone earthquakes is complicated by the combined effects of viscoelastic relaxation of earthquake-induced stresses in the upper mantle and time-dependent afterslip on the megathrust. We integrate geodetic observations and constraints on afterslip from small repeating earthquakes on the megathrust to better distinguish contributions from these two postseismic processes. We have developed a three-dimensional, spherical viscoelastic finite element model to study the postseismic deformation of the 2011 $M_w$9.0 Tohoku earthquake that has been recorded at unprecedented high resolution in space and time. We model stress-driven afterslip in a 2 km thick weak shear zone away from historic rupture zones on the megathrust. We model both the viscoelastic relaxation of the upper mantle and shear zone deformation with a transient Burgers body rheology. The transient Kelvin viscosity is assumed to be one order of magnitude lower than that of the Maxwell viscosity. Viscoelastic relaxation of the mantle wedge alone causes postseismic uplift and seaward motion in the upper plate, opposite to the pattern from relaxation of just the oceanic upper mantle. Afterslip on the fault produces uplift updip of the afterslip zone and subsidence over its downdip edge and mostly seaward motion above the afterslip zone. The best fit Maxwell viscosity of the shear zone at depths ≤50 km is $10^{17}$ Pa s, constrained by afterslip estimates from repeating earthquakes. The optimal viscosities of the deep weak shear zone, continental mantle wedge, and oceanic upper mantle are determined to be $5 \times 10^{17}$ Pa s, $3 \times 10^{19}$ Pa s, and $5 \times 10^{19}$ Pa s, respectively. The stress-driven afterslip in the shear zone is up to ~3.5 m in the first 2 years after the earthquake, equivalent to an $M_w$8.4. Our model reproduces the first-order pattern of the GPS observations both in horizontal and in vertical directions. Seafloor geodetic observations of subsidence and landward motions near the high-slip zone of the earthquake provide evidence for a low-viscosity asthenosphere below the oceanic lithosphere.

## 1. Introduction

In the last decade, several *M*8–*M*9 earthquakes have ruptured convergent boundaries around the world [*Kanamori*, 2014; *Lay*, 2014] for which rupture processes, coseismic slip, and postseismic deformation have been recorded by modern seismic and geodetic methods. Recorded postseismic crustal deformation following these megathrust earthquakes indicates that the upper plate mostly moves toward the trench, in the same direction as the coseismic displacement [e.g., *Pollitz et al*., 2008; *Panet et al*., 2010; *Ozawa et al*., 2012]. This is consistent with the expected motion from both afterslip on the megathrust and viscoelastic relaxation in the mantle wedge below the continental lithosphere. For the 2011 $M_w$9.0 Tohoku earthquake, seafloor geodetic measurements indicate that a few stations above the rupture zone near the trench moved landward, apparently due to viscoelastic relaxation of the oceanic upper mantle [e.g., *Watanabe et al*., 2014; *Sun et al*., 2014]. Decades after a great subduction zone earthquake, for example, after the 1960 $M_w$9.5 Chile [e.g., *Klotz et al*., 2001; *Wang et al*., 2007] and 1964 $M_w$9.2 Alaska [e.g., *Suito and Freymueller*, 2009] earthquakes, coastal areas move landward, indicative of the relocking of the megathrust, while inland area still move toward the trench due to enduring viscoelastic relaxation. Centuries after the earthquake, such as the 1700 $M_w$9 Cascadia earthquake [e.g., *McCaffrey et al*., 2013], the whole upper plate moves toward land consistent with interseismic elastic deformation about a locked subduction thrust [e.g., *Savage*, 1983].

*Wang et al*. [2012] propose that the interseismic earthquake cycle deformation is controlled by the interplay of three primary subduction zone processes, that is, continuous aseismic slip of the megathrust including afterslip, viscoelastic relaxation of earthquake-induced stresses in the upper mantle, and relocking of the

megathrust. At decadal to centennial timescales, the crustal deformation is controlled mainly by the viscoelastic relaxation of the upper mantle and relocking of the megathrust [e.g., *K. Wang et al*., 2003; *Hu et al*., 2004; *Suito and Freymueller*, 2009]. At short timescales (i.e., within a few years after the earthquake), the crustal deformation may be dominated by afterslip on creeping portions of the megathrust surrounding locked rupture asperities and downdip of the seismogenic zone. Dense geodetic and seismic networks are thus required to delineate the evolution of early afterslip. Postseismic deformation and seismicity following the 2011 $M_w$9.0 Tohoku earthquake have been recorded at unprecedented resolution in space and time at more than 1200 on-land continuous Global Positioning System (GPS) stations [*Ozawa et al*., 2012], seven ocean bottom GPS-Acoustic (GPS-A) stations [*Watanabe et al*., 2014; *Tomita et al*., 2015], and a dense seismic network [e.g., *Kato and Igarashi*, 2012; *Uchida and Matsuzawa*, 2013]. The high-quality geodetic and seismic data provide a unique opportunity to study the three-dimensional (3-D) rheological structure of the upper mantle and distribution and evolution of afterslip on the megathrust.

In the last few decades, a number of studies in NE Japan have revealed the structure and properties of the lithosphere and upper mantle [e.g., *von Huene et al*., 1994; *Zhao et al*., 1997; *Kawakatsu et al*., 2009; *Muto et al*., 2013], thermal structure of the subduction zone [e.g., *Peacock and Wang*, 1999; *Wada and Wang*, 2009], the paleoseismic evidence of previous great megathrust ruptures [e.g., *Minoura et al*., 2001; *Sawai et al*., 2008], and the distribution of coupling and frictional properties of the megathrust [e.g., *Hashimoto et al*., 2009; *Ghimire and Tanioka*, 2011]. These results provide the framework for models of postseismic deformation aimed at illuminating the rheology of the megathrust and upper mantle of NE Japan.

Several studies have explored the early postseismic deformation following the Tohoku earthquake. *Diao et al*. [2014] used a layered Earth model to explore both afterslip-only models and combined models of afterslip and relaxation in the viscoelastic upper mantle with a Maxwell rheology (a Maxwell viscosity $2\times10^{19}$ Pa s). They obtained afterslip of up to 3.8 m with more than 1 m down to depths >100 km, where the subduction interface may be coupled based on thermal models [e.g., *Wada and Wang*, 2009]. *Yamagiwa et al*. [2015] used a layered Earth model similar to that in *Diao et al*. [2014] except that they assumed a lower viscosity $9\times10^{18}$ Pa s in the upper mantle. In addition to the same large afterslip at greater depths (>100 km) as in *Diao et al*. [2014], they obtained afterslip in a reversed direction in areas in the vicinities of the coseismic rupture area. It has been a common feature in other models inverting for afterslip in an elastic half space or in a layered Earth that afterslip takes place to great depths [e.g., *Ozawa et al*., 2012; *Bedford et al*., 2013; *Lubis et al*., 2013; *Nishimura et al*., 2014]. *Johnson et al*. [2012] examined afterslip inversions in which rupture asperities from the Tohoku-Oki and previous earthquakes are not allowed to slip. To fit the 8 months cumulative postseismic displacements, they argue that afterslip likely occurred within the historical earthquake asperities. *Sun et al*. [2014] demonstrated the important role of viscoelastic relaxation in the upper mantle to produce observed landward motion near the trench. Details of their model will be discussed in section 5.1. We benefit from these previous studies to construct a more realistic finite element model and to carry out systematic tests on the contributions of stress-driven viscoelastic relaxation in a heterogeneous upper mantle and afterslip on the megathrust to the postseismic deformation of the 2011 Tohoku earthquake.

In this work, we present a finite element model of both the viscoelastic relaxation of the upper mantle and time-dependent afterslip driven by the stress changes from the 11 March 2011 $M_w$9.0 Tohoku earthquake in NE Japan. Afterslip at shallow depths is constrained by repeating earthquakes on the subduction megathrust [*Uchida and Matsuzawa*, 2013]. We then carry out a systematic exploration of the model rheology parameter space governing afterslip at greater depths and relaxation of continental (mantle wedge) and oceanic upper mantle. Optimal values of these three model parameters are determined from hundreds of test models by comparing the predicted surface displacements with the GPS and GPS-A data. After we obtain model parameters with the lowest misfit to GPS observations for this first-order configuration, we explore the effects of higher-order heterogeneities, such as the role of subduction of the Philippine Sea plate, the effect of a thin weak asthenosphere beneath the oceanic lithosphere [*Kawakatsu et al*., 2009], and contributions from poroelastic rebound in shallow layers of the continental and oceanic crusts and relaxation from weakened lower crust beneath the volcanic arc as reported in *Hu et al*. [2014]. Based on our findings, we discuss how improved understanding of the earthquake cycle deformation in northeast Japan may reconcile the historic pattern of coastal subsidence with long-term Holocene terrace uplift along the coast.

## 2. Data

### 2.1. GPS Data on Land

We obtained daily time series of more than 1200 GNSS (Global Navigation Satellite Systems) Earth Observation Network System (GEONET) stations that are processed in ITRF2005 [*Altamimi et al*., 2007] from the Geospatial Information Authority of Japan (GSI) [*Miyazaki and Hatanaka*, 1998] and of five International GNSS Service (IGS) stations in Korea, China, and Russia, from the Nevada Geodetic Laboratory (Nevada Bureau of Mines and Geology, Univ. of Nev., Reno, http://geodesy.unr.edu/index.php, last accessed on 07/28/2015) that are processed in ITRF2008 [*Altamimi et al*., 2011]. Because this work focuses only on the deformation associated with the 2011 event, we first summarize the approach of removing the pre-earthquake trends and deriving the postseismic displacements. For details of the analysis of the GPS time series the reader is referred to *Hu et al*. [2014]. First, we extract the GPS time series from 1998 to 2002 to estimate secular trends, annual and semiannual variations. There were only minor earthquake occurrences and few known transient events during this time window (only four $M_w$6.1–6.4 events between latitudes 36° and 42° in NE Japan). We fit the extracted time series with a function including static offsets, linear rates, annual and semiannual terms. After the constants of the function are estimated from the extracted time series, we remove the pre-earthquake trends and seasonal deformation from the postseismic time series starting on 12 March 2011. We then fit the postseismic time series of the 2011 event for each station with a function of logarithmic and exponential terms. We apply a grid-search method to estimate the characteristic time of logarithmic ($\tau_{\log}$) and exponential ($\tau_{\exp}$) terms that provide the best fit to time series of each station. The mean and ±1 standard deviation of the characteristic time constants are $\tau_{\log} = 0.3 \pm 0.5$ years and $\tau_{\exp} = 1.1 \pm 0.8$ years for the horizontal components and $\tau_{\log} = 0.6 \pm 0.6$ years and $\tau_{\exp} = 1.0 \pm 0.8$ years for the vertical component. Postseismic displacements between any two dates are then sampled from the fitted logarithmic and exponential functions to minimize uncertainties and effects of data gaps in the GPS time series. All the GPS stations are referenced to station FUKUE (station ID 950462), which is more than 1300 km from the 2011 rupture zone (solid yellow square in Figure 1c).

We use a two-dimensional quantization algorithm known as quadtree [*Welstead*, 1999] to select a subset of GEONET stations that are used to evaluate finite element model (FEM) test models. The advantages of the quadtree approach for the purpose of this work include that (1) the downsampling of densely spaced GEONET stations at larger distances from the rupture gives more weight to the near-field stations, scarce offshore GPS-A, and the few very far-field GPS stations; (2) this approach reduces local noise in GPS displacements; and (3) a smaller number of GPS stations saves computing time. The quadtree approach is commonly used for data reduction without losing significant information, such as in model inversions of interferometric synthetic aperture radar data [e.g., *Jónsson et al*., 2002]. In this procedure, the data space is equally divided into four quadrants. The mean and root-mean-square (RMS) scatter in each quadrant are calculated. If the RMS scatter about the mean is smaller than a given threshold, the station whose deformation is the closest to the mean is used to represent the data in that quadrant. If the RMS scatter exceeds the threshold, the quadrant is divided into four new quadrants and the algorithm is iterated until convergence is found at the given threshold for all remaining regions. The threshold (the RMS scatter divided by the mean) used to reduce the GEONET data in this work is 0.1 cm in areas between latitudes 36°N and 41°N (main rupture area) and more than 0.5 cm in the far field. Then we manually adjust a few GPS stations to have a spatial coverage that better preserves the first-order pattern of the recorded viscoelastic postseismic deformation. In the end, we selected 73 land stations based on the quadtree method from the more than 1200 GEONET stations. Note that we use the quadtree-sampled stations only to evaluate test models. After we select a model, we still use all GEONET stations to present the model results. In Figures 1a and 1b, red and black arrows represent those selected by the quadtree method and those not selected, respectively.

Two years after the 2011 event, the land stations recorded cumulative displacements of up to ~1.2 m in a similar direction as the coseismic motions (Figure 1a). Stations along the eastern coast underwent up to ~20 cm uplift, while inland areas experienced up to ~10 cm subsidence (Figure 1b). A Russian station more than 1000 km from the rupture zone moved ~4 cm toward the southeast (Figure 1c). Displacements of two Korean and two Chinese stations are ~1–2 cm toward the rupture zone except the farthest Chinese station in Shanghai, which has moved northeastward (Figure 1c). Three stations in the Philippine Sea plate (PSP) underwent a clockwise rotation with displacements of ~1 cm. A station more than 2000 km from the rupture area on the Pacific plate (PAC) moved ~1.5 cm to the northwest.

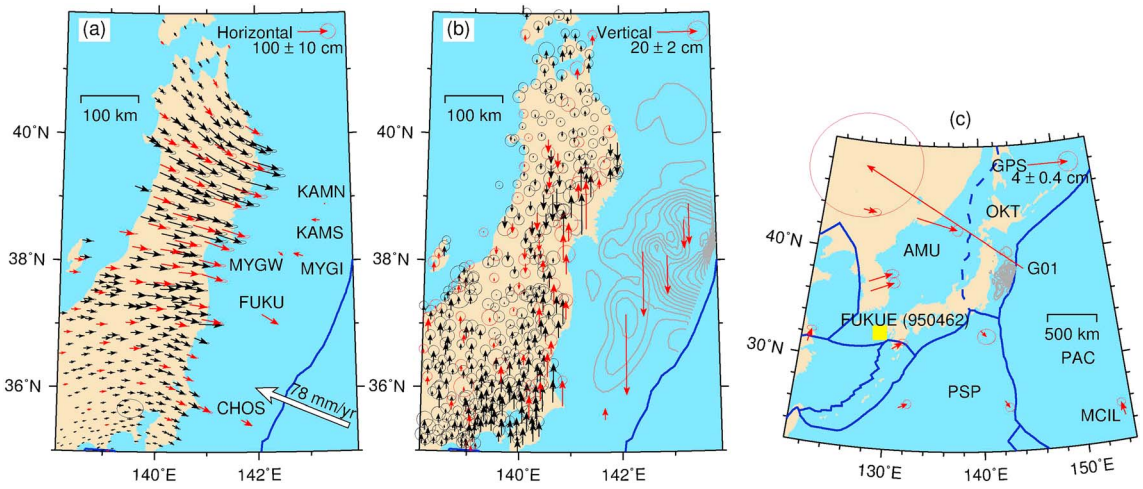


**Figure 1.** Postseismic GPS observations in the first 2 years following the 2011 Tohoku earthquake. (a) Horizontal and (b) vertical GPS displacements of GEONET and GPS-A stations. Red arrows represent the GPS stations selected to evaluate test models through quadtree method (see text for details). Black arrows are those not selected. (c) Horizontal postseismic GPS observations of five far-field IGS stations, one GPS-A station G01, and far-field GEONET stations in the Philippine Sea and Pacific plates. Displacements of G01 are averaged from 11 September 2012 to 17 October 2014 [*Tomita et al*., 2015]. Gray contours in Figures 1b and 1c are the coseismic rupture of the 2011 Tohoku earthquake at intervals of 5 m [*Iinuma et al*., 2012]. All the GPS displacements are corrected for interseismic deformation and are referenced to station FUKUE (ID 950462) whose location is shown by a solid yellow square in Figure 1c. PAC, OKT, AMU, and PSP denote the Pacific, Okhotsk, Amuria, and Philippine Sea plates, respectively.

### 2.2. Offshore GPS-Acoustic (GPS-A) Data

We compiled postseismic displacements of six GPS-A stations from the Japan Coast Guard and Tohoku University [*Watanabe et al*., 2014] and of one GPS-A station G01 on the Pacific plate (PAC) ~80 km from the trench from *Tomita et al*. [2015]. Because of the campaign-mode occupations of the GPS-A stations, we do not take the same detrending approach as in processing the continuous GEONET data. We remove the pre-earthquake velocities of the GPS-A stations reported by *Sato et al*. [2013] from the published 1 year and 2 years postseismic data [*Japan Coast Guard*, 2012; *Japan Coast Guard and Tohoku University*, 2013]. Because G01 was installed after the 2011 event, we subtract the plate motion of the Pacific plate (PAC) [*Altamimi et al*., 2011] from the time series and then calculate the postseismic displacements from 11 September 2012 to 17 October 2014 from the fitted linear trend. The postseismic displacements of the GPS-A stations are also referenced to station FUKUE (see section 2.1).

Two GPS-A stations KAMS and MYGI in the peak rupture zone and the G01 on the PAC started to move landward following the main shock, while the other four GPS-A stations moved seaward (Figure 1). Except for station CHOS with ~5 cm uplift, the other GPS-A stations in the upper plate underwent up to ~40 cm subsidence.

### 2.3. Repeating Earthquakes

It has been observed that some small asperities repeatedly initiate small *M*3–4 earthquakes with almost the exact same seismic waveforms on the megathrust [e.g., *Igarashi et al*., 2003; *Uchida and Matsuzawa*, 2013]. These earthquakes are called "repeating earthquakes." Based on the magnitude and focal mechanism of the repeating earthquakes, we can derive the slip history of the asperities from the repeating earthquakes [*Nadeau and Johnson*, 1998]. If we assume that areas surrounding the asperities aseismically slip by the same amount as the slip in the repeating earthquakes, we may derive the evolution of the aseismic afterslip over the megathrust near the locations of these repeating earthquakes. Using the same approach as reported in *Uchida and Matsuzawa* [2013], we extend their estimates of 300 day postseismic afterslip for an additional ~400 days (Figures 2a–2c). Within the first ~700 days after the 2011 event, the 60 km wide area along the downdip edge of the peak coseismic rupture zone (region 6) slipped on average by 103 cm. Asperities at the northern and southern edges of the main rupture area (regions 1–5, 7–11) slipped 7–93 cm. The repeating sequences that were active within the high-slip zone prior to the earthquake have failed to recur since [*Uchida and Matsuzawa*, 2013, their Figure 7d]. In these asperities (green and magenta rectangles in

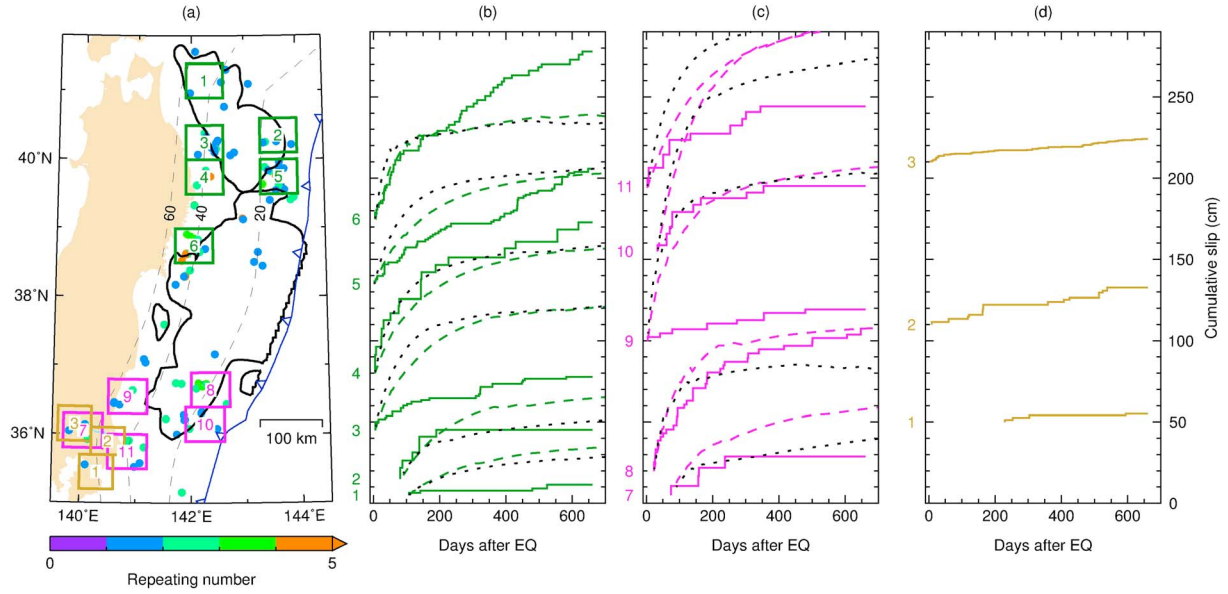


**Figure 2.** Historic asperities and cumulative afterslip evolution of the shallow megathrust in NE Japan. (a) Repeating earthquakes and historic asperities. Colored dots represent repeating earthquakes since the 2011 Tohoku earthquake with the color scale indicating the number of recurrences during the first ~700 days following the main shock. Thick black lines outline rupture areas of the 2011 event and previous events [*Yamanaka and Kikuchi*, 2004; *Iinuma et al*., 2012]. Modeled afterslip is only allowed outside of these inferred locked patches (solid black lines). Colored and numbered rectangles are fault areas with groups of repeaters along the megathrusts of the PAC (green and magenta) and the PSP (brown). (b) Cumulative afterslip of the PAC from repeating earthquakes after the 2011 earthquake in areas 1–6. (c) Afterslip of the PAC in areas 7–11. (d) Afterslip of the PSP in areas 1–3. Solid lines in Figures 2b–2d represent afterslip derived from repeating earthquakes. Dashed lines in Figures 2b and 2c represent predicted afterslip in a weak shear zone model of which the preferred viscosity is $10^{17}$ Pa s. Dotted lines in Figures 2b and 2c represent predicted afterslip with a shear zone viscosity $5 \times 10^{16}$ Pa s, half of the preferred value.

Figure 2). The average secular slip rate inferred from all the repeating earthquake sequences averaged in the same time window 1998–2002 as in processing the GPS time series (see section 2.1) is ~2.7 cm/yr, which is negligible compared to a few tens of centimeters a year of postseismic slip.

The rates of repeating earthquakes on the plate boundary thrusts of the PSP under the Okhotsk plate (OKT) and the PAC under the PSP are lower than those on the PAC-OKT boundary near the main rupture area of the 2011 earthquake. The asperities on the PSP-OKT boundary slipped by 5–23 cm within the same ~700 days after the earthquake (Figure 2d). The secular aseismic slip rate inferred from the repeating earthquakes before the 2011 event is only ~1.8 cm/yr.

## 3. Model Setup

### 3.1. Finite Element Model

The 3-D viscoelastic finite element model (FEM) used in this work is based on previous studies of Chile, Sumatra, and Cascadia subduction zones [*Wang et al*., 2012] and is described in *Hu et al*. [2014]. The model includes an elastic upper plate, an elastic subducting slab, a viscoelastic mantle wedge, and a viscoelastic oceanic upper mantle (Figure 3). Based on numerical modeling of other margins [e.g., *Hu et al*., 2004; *Hu and Wang*, 2012] and seismic studies on the structure of NE Japan [e.g., *Zhao et al*., 1997, 2009], we assume the elastic thicknesses of the continental and oceanic lithosphere to be 40 km and 80 km, respectively. After we obtain optimized rheological parameters for this simplified model constrained by the first-order pattern of GPS observations, we evaluate effects of rheological heterogeneities in the along-strike and depth directions. Unlike previous studies of afterslip which prescribe the kinematic motion of the fault, we use a weak shear zone representation of the megathrust to simulate the time-dependent, stress-driven afterslip. The shear moduli of the elastic lithosphere and viscoelastic upper mantle are 48 GPa and 64 GPa, respectively. The shear modulus of the weak shear zone is assumed to be 6.4 GPa, one order of magnitude lower than that of the viscoelastic upper mantle, to better approximate the rapid afterslip on the fault. If we use the same 64 GPa in the shear zone as that of the upper mantle, the viscosity of the shear zone would be required to be extremely low to produce enough afterslip, and the modeled afterslip would be

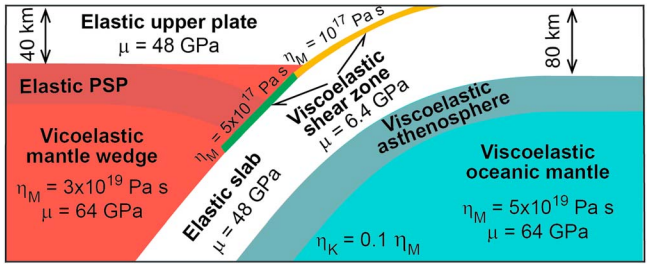


**Figure 3.** Conceptual representation of the finite element model. The finite element model includes an elastic upper plate and elastic subduction slab (white color blocks), viscoelastic mantle wedge (red), oceanic mantle (cyan), and shear zone along the plate interface (green and brown). Elastic subducting Philippine Sea Plate (PSP) and viscoelastic asthenosphere beneath the oceanic lithosphere (shaded areas, not to scale) will be discussed in section 5. $\mu$ is the shear modulus. The shown steady state viscosity values $\eta_M$ are 10 times the corresponding transient viscosity $\eta_K$. The viscosities shown represent the determined values found in the three-parameter optimization described in section 4.2.

short-lived (e.g., at timescales of a few days). A lower shear modulus allows the rapid afterslip to endure for a reasonably long time (e.g., more than a few years). The Poisson's ratio and rock density are assumed to be 0.25 and $3.3 \times 10^3$ kg/m$^3$, respectively, for the entire domain.

The steady state deformation of viscoelastic rocks by dislocation creep may be represented by a laboratory-determined power law rheology, that is, a relationship between the strain rate and differential stress to the power $n$, where $n$ tends to be about 3 for olivine under mantle conditions. The effective viscosity in materials deforming by dislocation creep decreases with increasing differential stress and is a function of rock properties (including composition, grain size, and fluid content), initial stresses, and temperature. Dislocation creep has been inferred to dominate flow in the lower crust and upper mantle based on experimental evidence, microstructural studies of exhumed deformed rocks, and observations of seismic anisotropy [*Bürgmann and Dresen*, 2008]. If stress levels are low and grain sizes small, ductile rock deformation may be dominated by diffusion creep and can be described by a linear Newtonian relationship between the strain rate and stress in which viscosity is stress independent. It has been argued that the Newtonian rheology may be adequate in modeling viscoelastic deformation due to small stress perturbations at timescales of $10^1$–$10^4$ years [e.g., *Melosh and Raefsky*, 1983; *Wang*, 2007]. In such a case an effective Newtonian viscosity can adequately describe the viscoelastic flow. Viscous relaxation by power law flow was found to match the observed rapid decay of postseismic deformation observed following the 1992 Landers and 1999 Hector Mine earthquakes [*Freed and Bürgmann*, 2004] and the 2002 Denali earthquake [*Freed et al.*, 2006]. A linear biviscous Burgers body rheology, possibly representing transient creep following a stress step, has also been found to capture the rapidly decaying deformation following these and other strike-slip earthquakes [e.g., *Pollitz*, 2003, 2005; *Hearn et al.*, 2009] and has been used to model time-dependent relaxation following recent subduction zone events [e.g., *Pollitz et al.*, 2008; *Hoechner et al.*, 2011; *Hu and Wang*, 2012; *Meade et al.*, 2013; *Mikhailov et al.*, 2013; *Trubienko et al.*, 2014; *Broerse et al.*, 2015; *Wiseman et al.*, 2015]. *Freed et al.* [2010, 2012] combined steady state power law rheology and biviscous transient creep to better reproduce the earliest short-term postseismic deformation of the 1999 Hector Mine earthquake. Models employing power law rheology require knowledge of the three-dimensional distribution of composition, temperature, grain size, fluid content, and ambient stress and are thus difficult to parameterize.

In this work, we rely on the biviscous Burgers body rheology to represent the viscoelastic relaxation of the upper mantle and plate boundary shear zone. The biviscous rheology captures the apparent rapid decay of effective viscosities over the course of a few years. Dislocation creep via a power law rheology and/or a transient rheology may be responsible for this behavior. Different values of the ratio of the steady state Maxwell viscosity $\eta_M$ over the transient Kelvin viscosity $\eta_K$ have been assumed in theoretical models or have been obtained in laboratory experiments in geophysical studies, for example, ~1–6 in *Chopra* [1997], 10 in *Sabadini et al.* [1985], 20 in *Pollitz et al.* [2006, 2008], and 29 in *Pollitz* [2003]. In this work, $\eta_K$ in all the viscoelastic elements is assumed to be one order of magnitude lower than $\eta_M$. The viscosity values provided hereafter in this paper indicate the steady state viscosity except when explicitly stated otherwise. For simplicity, we assume that the shear modulus in the Maxwell element is the same as that of the Kelvin element.

The coseismic slip distribution of the earthquake derived by *Iinuma et al.* [2012] is kinematically prescribed using the split node method [*Melosh and Raefsky*, 1981]. Except for the top free surface, the other five model boundaries are free in the tangential directions and are fixed in the normal direction. Domain boundaries are

more than 1000 km from the rupture zone in the horizontal directions. The bottom of the model is at 500 km depth. The setup of the model boundaries has negligible effects on the deformation of the focus area.

Following the approach of developing the FEM mesh in *Hu and Wang* [2012], we manually derived 32 latitude-parallel profiles based on published slab geometry data [*Nakajima and Hasegawa*, 2006; *Zhao et al*., 2009; *Hayes et al*., 2012], relocated seismicity [*Engdahl et al*., 1998], and locations of the trench [*Bird*, 2003] and the arc. Our slab geometry is similar to that used in *Iinuma et al*. [2012]. These latitude-parallel profiles were then used to construct the 3-D finite element mesh. It consists of 147,867 nodal points in 17,408 27-node quadratic elements. The element size is on the order of 0.1 km near the fault and up to 500 km farther away. The parallel modeling finite element code PGCvesph was developed at the Pacific Geoscience Centre, Geological Survey of Canada [e.g., *Hu and Wang*, 2012; *Wang et al*., 2012; *Sun et al*., 2014]. Each test model took ~5 h on an eight-core Intel Xeon 2GHz CPU, 8 Gb RAM computer.

### 3.2. Stress-Driven Afterslip

The study of the distribution and evolution of subduction earthquake afterslip has been limited by the capability of existing geodetic and seismic networks and lack of direct observations offshore. We take advantage of the dense terrestrial networks as well as geodetic observations offshore in NE Japan to better characterize the afterslip properties following the 2011 earthquake. A conventional way to derive the distribution of the afterslip is to invert the surface deformation observed mostly on land with or without removing the effects of the viscoelastic relaxation of the upper mantle in an elastic half space [*Okada*, 1985] or layered Earth [ *R. Wang et al*., 2003]. This approach ignores the viscoelastic response to time-dependent afterslip, which is significant and usually results in large estimates of afterslip at greater depths [e.g., *Sato et al*., 2010; *Bedford et al*., 2013; *Lubis et al*., 2013; *Sato et al*., 2013; *Diao et al*., 2014]

During a subduction zone earthquake, seismogenic portions of the fault have velocity-weakening behavior via which dynamic slip initiates and propagates along the earthquake rupture. Neighboring portions that exhibit velocity-strengthening behavior resist the propagation of coseismic rupture. Therefore, stresses relieved from the seismogenic zone are transferred to the neighboring portions. After the earthquake, the resultant relaxation and transfer of stresses along the fault cause aseismic afterslip that rapidly decays with time. This frictional behavior of the fault can be explicitly modeled using the rate- and state-dependent friction law [e.g., *Ruina*, 1983; *Dieterich*, 1994]. Our shear zone approach is used not to model the frictional properties of the fault [e.g., *Johnson et al*., 2006; *Barbot et al*., 2009; *Rousset et al*., 2012] but to approximate the equivalent effects of the stress-driven afterslip on the surface deformation [*Hearn et al*., 2002, 2009]. Here we rely on the fast relaxation of a narrow biviscous viscoelastic shear layer along the plate interface to model the response of aseismically slipping portions of the fault to the coseismic stress changes. We allow for such stress-driven afterslip both on uncoupled sections of the megathrust at seismogenic depths and downdip of the seismogenic zone. Whether the viscosities of the shear zone obtained in this work indicate real physical properties of the fault is beyond the scope of this paper.

We follow the example of *Hearn et al*. [2002] who applied a weak viscoelastic shear zone to simulate afterslip in a model of the postseismic deformation of the 1999 $M_w$7.5 İzmit earthquake, finding that a viscous fault zone model fit geodetic data equally well as one using velocity-strengthening frictional slip. We use a low-viscosity shear layer along the fault to simulate the stress-driven afterslip (thin brown and green layers in Figure 3). The modeled afterslip is computed by differencing the displacements of the bottom of the shear zone layer and its corresponding top surface. Thickness of the shear layer scales with its viscosity; that is, a thinner shear zone requires a lower viscosity to produce the same modeled afterslip. Considering the deformation gradient near the fault and the element size needed to reduce numerical artifacts, we used a 2 km thick shear layer. We assume that locked regions of the fault within the seismogenic depth range can be constrained by the distribution of known historical asperities along the plate margin (thick black lines in Figure 2a) [*Yamanaka and Kikuchi*, 2004; *Uchida and Matsuzawa*, 2013]. The viscosity of the model plate boundary is several orders of magnitude higher in these locked regions, such that simulated afterslip only takes place outside of the historical asperities illustrated in Figure 2a. We consider a two-layered viscosity structure separated at 50 km depth to account for the change in fault properties at the base of the seismogenic region of the plate boundary fault. For simplicity, we assume no along-strike variations in the rheological properties of the shear zone. The along-strike boundaries of the shear zone is assumed to be between latitudes of 33.5°N and 43°N, extending from the main rupture area by ~200 km.

### 3.3. Afterslip in the Seismogenic Zone Constrained From Repeating Earthquakes

Based on the slip evolution derived from repeating earthquakes at depths ≤50 km (solid lines in Figures 2b and 2c), we vary the viscosity in the shallow weak shear zone by trial and error such that the modeled afterslip in the shear zone matches the overall pattern of the slip of the repeating earthquakes. In this section, the rest of the model domain including the upper mantle is assumed to be elastic because the deformation in the shear zone is controlled mainly by the relaxation of coseismically induced stresses. Including the effects of the viscoelastic relaxation of the upper mantle results in an increase in the modeled afterslip only by less than ~10%. Our preferred test model with a viscosity of $10^{17}$ Pa s in the shallow shear zone produces a good fit to the observed afterslip of the various fault segments (dashed lines in Figures 2b and 2c). The unit thickness viscosity of the shear zone at seismogenic depths is thus $5 \times 10^{16}$ Pa s. We purposely allow for an overestimated afterslip on segments 8–11 in the south, that is, modeled afterslip in the first 700 days is up to ~100 cm larger than that derived from repeating earthquakes (Figure 2c), to take into account the contribution of several *M*6–7 aftershocks in this region that occurred within a month after the main shock. The overestimate at segment 3 is probably due to the idealized location of the boundary of the locked region in this work. We do not further modify the locked area of the megathrust allowed to slip to further improve the fit to the repeater data.

Lowering the viscosity of the shallow shear zone by a factor of 2 (dotted black lines in Figures 2b and 2c) produces a similarly good fit to the observed afterslip of repeating earthquakes as in the model of the preferred viscosity of $10^{17}$ Pa s. The unit viscosity defined as the viscosity divided by the thickness of the shear zone is thus $0.5 \times 10^{17}$ Pa s/km. If the viscosity is larger than $10^{18}$ Pa s or less than $10^{16}$ Pa s, the fit to the repeating earthquake data becomes dramatically worse (results not shown). The preferred viscosity in the shallow shear zone is rather tightly constrained.

## 4. Model Results

In this section, we present the results of systematic tests varying the viscosities of the deep shear zone (depths of 50–100 km), the continental mantle wedge and the oceanic upper mantle. We then illustrate how well the determined lowest misfit model fits the GPS observations, both in the near-field and in the far-field areas. Since the viscosity of the shallow shear zone has already been determined to be $10^{17}$ Pa s by the repeating earthquakes (section 3.3), we determine the best fit viscosities of the three other rheological elements; the deep shear zone, mantle wedge, and oceanic upper mantle. We assume that the transient Kelvin viscosity ($\eta_K$) is one order of magnitude lower than that of the steady state Maxwell viscosity ($\eta_M$). The three $\eta_M$ to be determined make systematic tests manageable with respect to computing time. We apply a systematic grid-search approach to determine these viscosities. Based on studies of earthquake cycle deformation of other margins [e.g., *K. Wang et al*., 2003; *Hu et al*., 2004; *Suito and Freymueller*, 2009; *Hu and Wang*, 2012], we vary the viscosity of the deep shear zone ($\eta^S$) in a range of $10^{16}$–$10^{20}$ Pa s, the mantle wedge ($\eta^W$) between $10^{18}$–$10^{21}$ Pa s, and the oceanic upper mantle ($\eta^O$) over $10^{18}$–$10^{22}$ Pa s. We started with a coarse grid and then evaluated the best fitting area with a much finer grid. In the end, we constructed more than 700 test models with different combinations of the three viscosities.

For each test model, we calculate its misfit to the observed cumulative postseismic displacements of the stations downsampled with the quadtree method (section 2.1) as defined in (1).

$$\text{misfit} = \sum_{i=1}^{73} \sum_{t=1}^{4} \left| \left( G_i^t - M_i^t \right) \right| + \sum_{i=1}^{6} \sum_{t=1}^{2} w \left| \left( O_i^t - M_i^t \right) \right| \quad (1)$$

where *M* represent model predictions, *G* and *O* are land GPS and offshore GPS-A data, respectively, *i* and *t* represent station number and time step, respectively, and *w* is the weight assigned to the GPS-A data. For continuous land GPS, we use four equally spaced time steps covering the first 2 years. For offshore GPS-A in the upper plate, we consider two time periods, spanning years one and two, from the published data (section 2.2). Although the weighting factor $w = 1$ is used in evaluating the test models, different *w* will be examined to study the fit to these GPS-A stations in section 5.1.

Averaged misfit (AMF) is the total misfit in (1) divided by the number of stations. Misfits of the displacements in all three components are calculated separately to evaluate the fit to individual components. We do not use the weighted $\chi^2$ fit to evaluate test models, because postseismic displacements are already calculated through the fitted curve to GPS observations, which takes into account uncertainties of the GPS time series, and because the misfit is much larger than the measurement uncertainties (although much smaller than the signal).

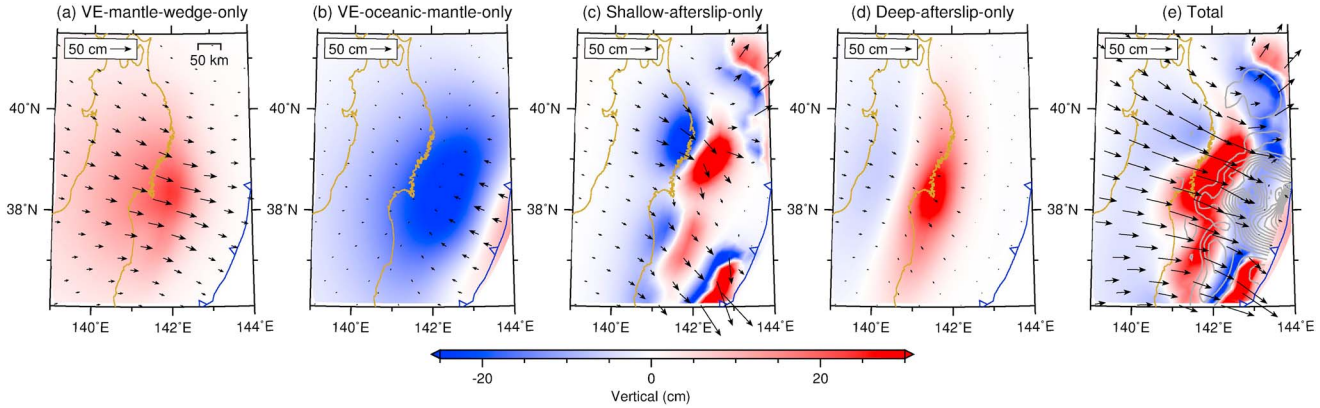


**Figure 4.** Separated contributions of relaxation in the rheological elements to the modeled surface deformation. Viscosities of the rheological elements are the same as that in the LAM (Figure 6b). Black arrows and contours represent cumulative 2 years horizontal and vertical postseismic displacements, respectively. Solid brown lines represent coast lines. Gray contours in Figure 4e represent coseismic slip contours of the 2011 earthquake [*Iinuma et al.*, 2012]. (a) Surface deformation only due to the viscoelastic relaxation of the continental upper mantle and no afterslip in the shear zone. The oceanic upper mantle is assumed to be elastic in this test. (b) Surface deformation only due to the viscoelastic relaxation of the oceanic upper mantle and no afterslip in the shear zone. The continental upper mantle is elastic. (c) Surface deformation only due to the afterslip in the shallow shear zone (≤50 km), no afterslip >50 km and no viscoelastic relaxation in the continental and oceanic upper mantle. (d) Surface deformation only due to the afterslip in the deep shear zone (50–100 km), no afterslip ≤50 km and no viscoelastic relaxation in the continental and oceanic upper mantle. (e) Surface deformation due to both the viscoelastic relaxation in the upper mantle and afterslip in the shallow and deep shear zone.

### 4.1. Contributions of Afterslip and Upper Mantle Relaxation to Surface Deformation

Viscoelastic postseismic surface deformation strongly depends on the distance to the stress perturbation source and the viscoelastic flow pattern after the earthquake. The three rheological elements, a narrow shear zone accommodating afterslip (0–100 km depths), the continental mantle wedge, and the oceanic upper mantle make different contributions to the postseismic displacement components. In this section, we study the individual effects of these three rheological elements on the surface deformation. Note that in the following forward models stress-driven shallow afterslip (≤50 km) is constrained by repeating earthquakes as shown in Figure 2 and is fixed (see section 3.3). In the next section, we carry out systematic tests in the model parameter space and determine the optimized viscosities of the mantle wedge, oceanic upper mantle, and deep weak shear zone.

We study the individual effects by allowing viscoelastic relaxation only in one rheological unit, while the other three units are defined to be "elastic" (infinite viscosity). Viscosities of the rheological elements are based on a lowest averaged misfit model (LAM) obtained in section 4.2. Viscoelastic relaxation of stresses in the mantle wedge causes seaward motion in the upper plate and uplift mostly on land (landward of the downdip edge of the rupture zone) (Figure 4a). The oceanic upper mantle produces a reversed pattern of the surface deformation to that of the mantle wedge, that is, landward motion mostly close to the trench, modest seaward motion on land, and subsidence mostly offshore (Figure 4b). The difference in the surface deformation is related to the fact that during the coseismic rupture the hanging wall (the continental side) moves seaward while the footwall (the oceanic side) moves landward. Therefore, the relaxation of coseismically induced stresses in the mantle wedge and oceanic mantle causes material flow in a reversed pattern in these two units. Deformation due to the shallow afterslip in the seismogenic zone (depths ≤50 km) is more heterogeneous, depending on the magnitude and distribution of the stress-driven afterslip on the fault (Figure 4c). Shallow afterslip produces overall seaward surface deformation, a pattern similar to that of the mantle wedge. The pattern of the vertical deformation is uplifted roughly updip of the afterslip zone and subsidence over the downdip edge of the afterslip zone. Deformation due to the deep afterslip (depths 50–100 km) produces up to ~10 cm seaward motion, up to ~5 cm uplift along the eastern coast and up to ~3 cm subsidence at the western coast, by 2 years after the earthquake (Figure 4d). The total effect is a combination of these four processes (Figure 4e).

We summarize the effects of the individual rheological elements as follows. For the horizontal components, the viscoelastic relaxation of the mantle wedge and deep afterslip on the fault control the postseismic seaward motion mainly on land, while the relaxation of the oceanic upper mantle and shallow afterslip on the fault controls the deformation mainly near the trench. For the vertical components, the mantle wedge

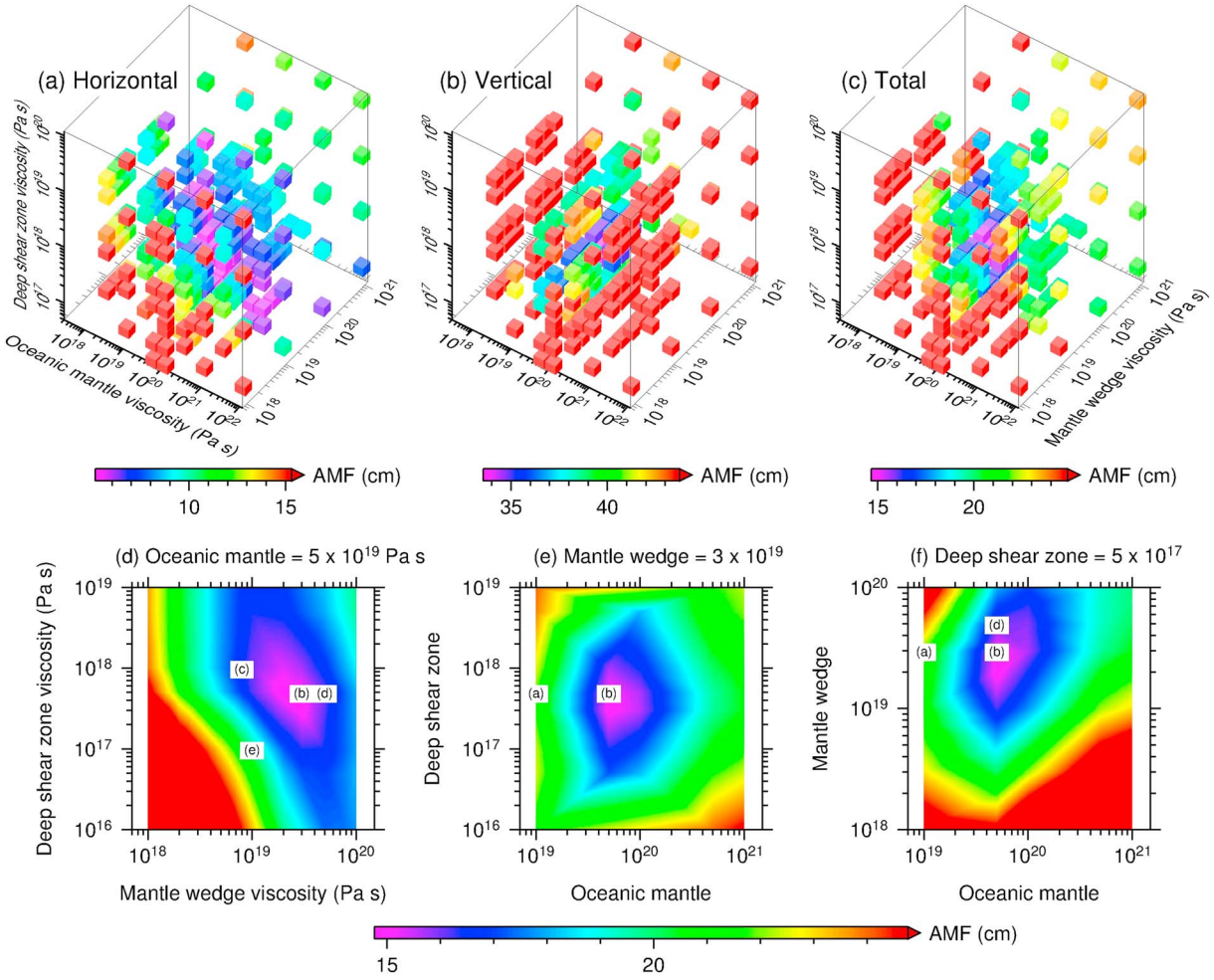


**Figure 5.** Misfit of test models and trade-off between the upper mantle rheology and deep shear zone rheology. Averaged misfit (AMF, from equation (1)) is calculated from (a) horizontal, (b) vertical, or (c) both horizontal and vertical displacements. Trade-offs of model parameters in this work are displayed as the relationship between viscosity values in any two of the three rheological elements, the oceanic upper mantle, mantle wedge, and deep shear zone, while the viscosity of the third is fixed to the LAM value. (d) The viscosity of the oceanic mantle is fixed at $5 \times 10^{19}$ Pa s, and viscosities of the mantle wedge and deep shear zone are variable. (e) The viscosity of the mantle wedge is fixed at $3 \times 10^{19}$ Pa s. (f) The viscosity of the deep shear zone is fixed at $5 \times 10^{17}$ Pa s. Misfits of test models labeled in Figures 5d–5f are plotted in Figure 6.

produces uplift in areas above the viscoelastic mantle wedge. Relaxation of the oceanic upper mantle produces uplift close to the trench and subsidence farther inland. Afterslip produces uplift updip of the afterslip zone and subsidence downdip.

### 4.2. Rheology of Upper Mantle and Deep Afterslip

In this section, we first study the overall pattern of deformation in the three-parameter space. We then report the trade-off effects between the three rheological elements on the surface deformation. In all the models discussed below, the shallow fault zone parameterization is kept the same (see section 3.3).

If we consider the misfit only in the horizontal GPS displacements (Figure 5a), the viscosity of the mantle wedge $\eta^W$ is fairly well constrained within a range of ~1–7 $\times 10^{19}$ Pa s while acceptable viscosities of the oceanic upper mantle and deep shear zone vary over much larger ranges ($\eta^O = 5 \times 10^{19}$ to $10^{21}$ Pa s and $\eta^S$ in a range of several orders of magnitude). The significant sensitivity to the mantle wedge viscosity indicates that the continental surface deformation in the horizontal direction may be controlled mainly by the viscoelastic relaxation of the mantle wedge. Relaxation of the other two units, the deep shear zone and oceanic upper mantle, are not as easily resolved. Note that a model providing a good fit to the horizontal components may fit the vertical component poorly. For example, the test model ($\eta^O = 10^{19}$ Pa s, $\eta^W = 3 \times 10^{19}$ Pa s

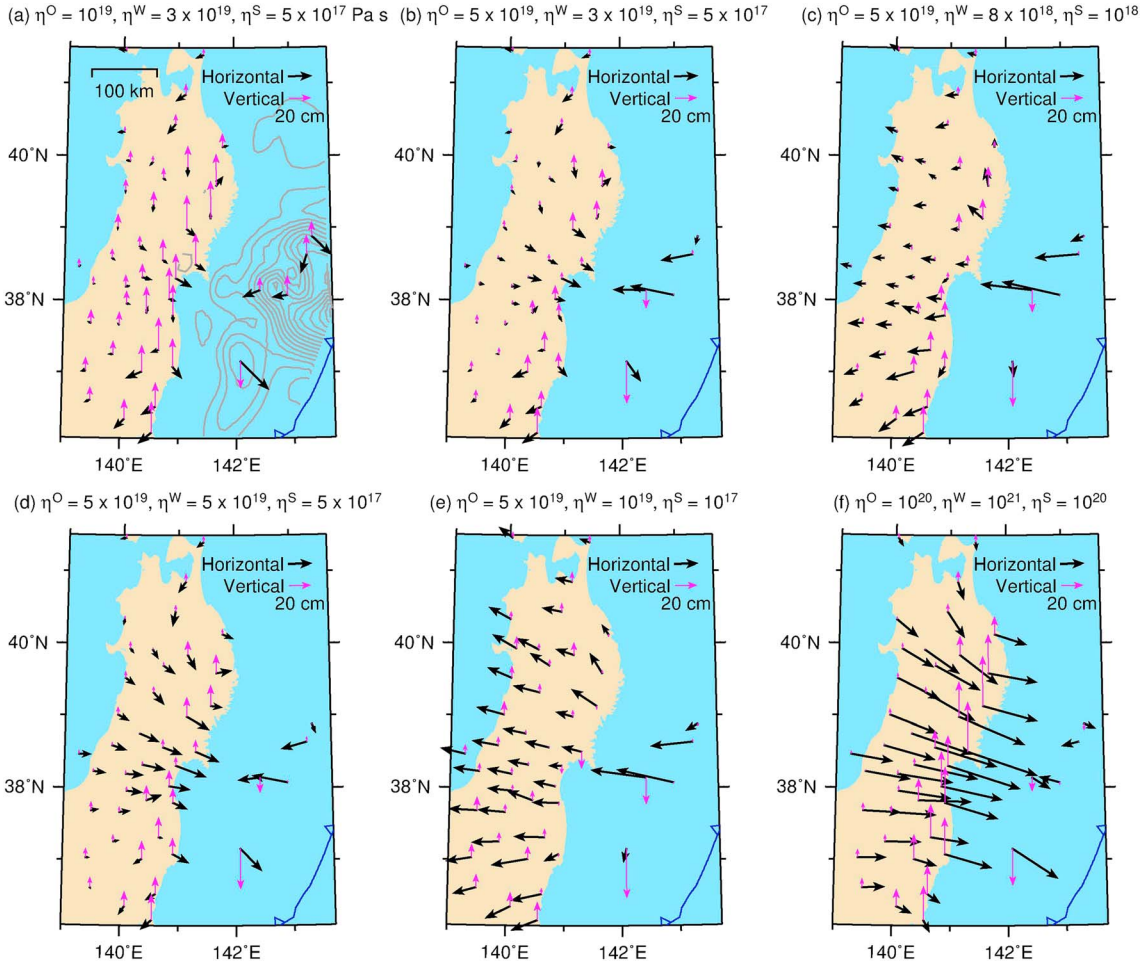


**Figure 6.** Residuals of 2 years postseismic displacements in six test models (a–f). Residual is defined as observed displacements at stations selected by the quadtree method (red arrows in Figure 1) minus model-predicted values. Viscosities of each rheological unit of these six models are illustrated in Figures 5d–5f and are also labeled on top of each plot. $\eta^O$, $\eta^W$, and $\eta^S$ represent steady state viscosities of the oceanic upper mantle, mantle wedge, and deep shear zone, respectively. Black and magenta arrows represent the horizontal and vertical components, respectively. The test model in Figure 6b is the lowest averaged misfit model (LAM).

$\eta^S = 5 \times 10^{17}$ Pa s) produces a good fit to the horizontal component but results in a poor fit to the vertical component (large vertical misfit denoted by magenta arrows in Figure 6a).

If we consider the misfit only in the vertical direction (Figure 5b), acceptable fit to the vertical component requires $\eta^S = 3\text{–}10 \times 10^{17}$ Pa s and $\eta^O = 5\text{–}10 \times 10^{19}$ Pa s while $\eta^W$ can vary over a larger range $5 \times 10^{18}$ to $10^{20}$ Pa s. A weaker deep shear zone, featuring larger modeled afterslip at depths >50 km, results in the larger uplift near the eastern coast and subsidence farther inland, a pattern similar to the observed vertical GPS as shown in Figure 1b.

The sum of the horizontal and vertical misfit reconciles the fit to both horizontal and vertical components of GPS observations. A linear combination of the horizontal and vertical misfits results in a bias in selecting the best fit models because the vertical displacements are overall about 5 times smaller than the horizontal displacements. We use the sum of horizontal misfits and 5 times the vertical misfit to evaluate the total effect of the test models. The combined misfit determines viscosities of all the three rheological elements in narrow ranges, that is, $\eta^W = \sim 0.8\text{–}5 \times 10^{19}$ Pa s, $\eta^S = \sim 2\text{–}20 \times 10^{17}$ Pa s, and $\eta^O = \sim 0.3\text{–}1 \times 10^{20}$ Pa s (Figure 5c). Viscosities in the test model with the lowest AMF (LAM) are $\eta^W = 3 \times 10^{19}$ Pa s, $\eta^S = 5 \times 10^{17}$ Pa s, and $\eta^O = 5 \times 10^{19}$ Pa s. Note that the LAM is also the model that produces the best fit to the vertical component (the model of the lowest AMF in Figure 5b). The unit thickness viscosity of the deep shear zone is thus $2.5 \times 10^{17}$ Pa s, five times larger than that of the shear zone at seismogenic depths (<50 km).

In order to better estimate the range of acceptable viscosities shown in Figure 5c, we study the trade-off of any two rheological elements while keeping the third fixed at the best fit value in the LAM (Figures 5d–5f). If

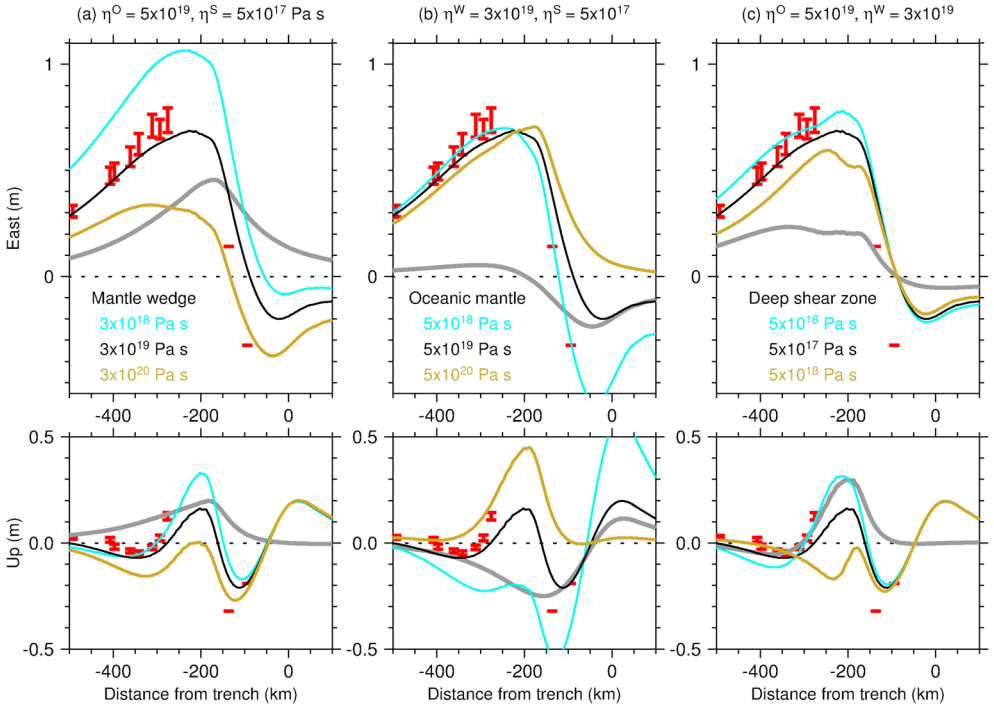


**Figure 7.** Sensitivities of the surface deformation to the viscosity change in the (a) mantle wedge, (b) oceanic upper mantle, and (c) deep shear zone. Two years postseismic displacements are plotted along a surface profile at latitude 38°N. Top and bottom images are East and upward directions, respectively. Red error bars represent observations at GEONET and GPS-A within 20 km of the profile line. In each column, the viscosity of one rheological element is varied, while the other two rheological elements are fixed at the same viscosities as in the LAM (labeled at the top). Color coding of the lines representing models of different viscosities is described in the insert text. Gray lines in Figures 7a and 7b represent the same test models as shown in Figures 4a and 4b in which the viscosity of one rheological unit is at the same value as in the LAM (black color), while the other two rheological elements are assumed to be ELASTIC (infinite viscosity). Gray lines in Figure 7c are the combined effects of Figures 4c and 4d. Black lines are the same LAM in all three columns.

$\eta^O$ is fixed at $5 \times 10^{19}$ Pa s, Figure 5d indicates that $\eta^W$ is anticorrelated with $\eta^S$; that is, a higher $\eta^W$ requires a lower $\eta^S$ to produce the same low misfit. The anticorrelation is due to the similar contributions to the surface deformation by the relaxation in the mantle wedge and deep afterslip. Two test models with about the same AMF of 16 cm produce a comparably good fit to GPS observations as the LAM (Figures 6c and 6d). Test models of larger AMF result in dramatically poorer fit to GPS observations (e.g., Figure 6e). Figure 5d indicates that acceptable viscosity ranges are $\eta^W = \sim 0.8\text{–}5 \times 10^{19}$ Pa s and $\eta^S = \sim 0.2\text{–}2 \times 10^{18}$ Pa s. If $\eta^W$ is fixed at the same $3 \times 10^{19}$ Pa s as in the LAM, there is no obvious pattern of the trade-off between $\eta^O$ and $\eta^S$ (Figure 5e). The acceptable viscosity range of $\eta^O$ is $\sim 0.3\text{–}1 \times 10^{20}$ Pa s to produce a similarly good fit to observations as the LAM. If $\eta^S$ is the same $5 \times 10^{17}$ Pa s as in the LAM, $\eta^W$ positively trades off with $\eta^O$; that is, a higher $\eta^W$ requires also a higher $\eta^O$ to produce the same good fit to observations (Figure 5f). This is probably due to the reversed contributions of these two processes to the surface deformation. Figure 5f illustrates the same viscosity range of $\eta^W$ and $\eta^O$ as discussed above.

We further study the rheological effects on the postseismic crustal deformation by varying the viscosity of one unit while fixing the viscosities of the other two at the preferred values in the LAM. If $\eta^S$ and $\eta^O$ are fixed at the preferred values in the LAM, that is, $5 \times 10^{17}$ Pa s and $5 \times 10^{19}$ Pa s, respectively, a lower $\eta^W$ results in overall more significant seaward motion and more uplift, mostly in the land area (Figure 7a). Areas near the trench, particularly the vertical component, are less affected. In all the three test models, areas within ~100 km to the trench move toward land. Note that the relaxation of the mantle wedge alone, that is, when shear zone and oceanic upper mantle are "elastic," produces wholesale seaward motion and uplift in the upper plate (Figure 4a and gray lines in Figure 7a).

If $\eta^W$ and $\eta^S$ are fixed at the preferred values in the LAM, that is, $3 \times 10^{19}$ Pa s and $5 \times 10^{17}$ Pa s, respectively, the change in $\eta^O$ affects the surface deformation mainly offshore (Figure 7b). The striking feature is that the

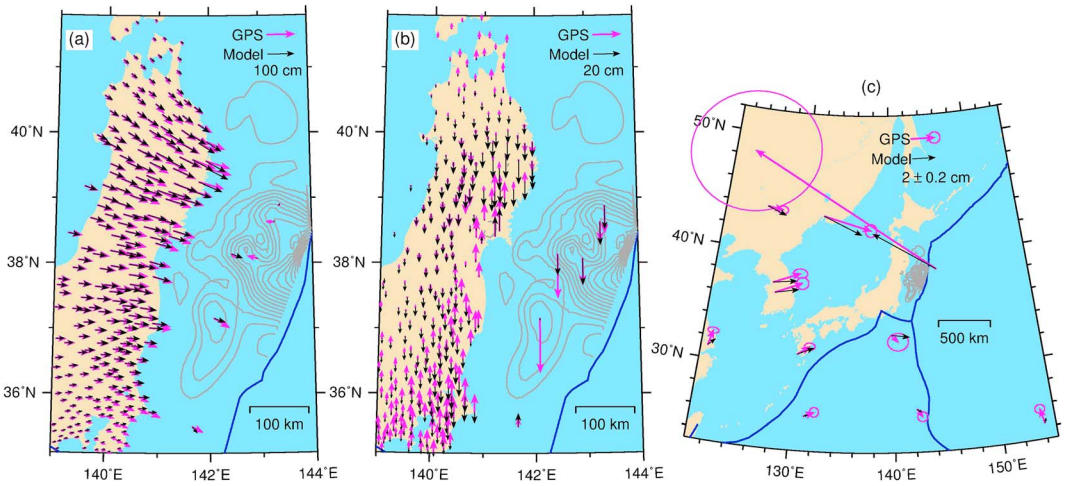


**Figure 8.** Comparison of GPS observations 2 years after the 2011 earthquake with the LAM. Magenta and black arrows represent GPS observations and model-predicted displacements, respectively. (a) Horizontal displacements. (b) Vertical displacements. (c) Comparison of very far-field GPS observations with model-predicted displacements.

oceanic upper mantle affects a much broader area with more dramatic change in the vertical deformation compared to those of the mantle wedge and shear zone relaxation (bottom images of Figure 7). The horizontal surface deformation on land is less affected by the viscosity change in $\eta^O$ (top image of Figure 7b). Landward motion near the trench may be reversed in test models of a high $\eta^O$ (e.g., brown lines Figure 7b).

If $\eta^O$ is up to one order of magnitude lower than that of the LAM (cyan lines in Figure 7b), effects of the oceanic upper mantle dominate and result in large landward motion and subsidence near the trench. This low $\eta^O$ model fits the GPS-A data much better, which indicates that the rheological structure of the oceanic upper mantle may be more complicated than in the models we have considered so far. Alternatively, parts of the coseismic rupture may not yet have relocked yet and do not produce repeating earthquakes that would provide clear evidence of creep. We will discuss possible processes such as including a weak asthenosphere beneath the oceanic lithosphere to better reproduce the landward motion of GPS-A sites in section 5.1.

If $\eta^W$ and $\eta^O$ are fixed at the preferred values in the LAM, that is, $3\times10^{19}$ Pa s and $5\times10^{19}$ Pa s, respectively, changes in $\eta^S$ affect the surface deformation mainly near the downdip edge of the rupture zone where the afterslip takes place (Figure 7c). The change in $\eta^S$ produces negligible change in the surface deformation near the trench and beyond on the oceanic side. A lower $\eta^S$, that is, larger modeled deep afterslip, produces more seaward motion, more uplift in the eastern coast area, and more subsidence further inland (Figure 7c).

### 4.3. Lowest AMF Model (LAM)

After evaluating the model space and the effects of each rheological unit, we are now ready to describe the predictions of the lowest averaged-misfit model obtained from the systematic tests discussed in section 4.2. For the combined effects as shown in Figure 5c, viscosities of the deep shear zone, mantle wedge, and oceanic upper mantle in the lowest AMF model (LAM) are $\eta^S=5\times10^{17}$ Pa s, $\eta^W=3\times10^{19}$ Pa s, and $\eta^O=5\times10^{19}$ Pa s, respectively (Figure 6b). The obtained mantle wedge viscosity of $3\times10^{19}$ Pa s in this work is consistent with studies of other subduction zones [e.g., *Hu et al*., 2004; *Suito and Freymueller*, 2009; *Hu and Wang*, 2012; *Wiseman et al*., 2015]. The LAM reproduces the first-order pattern of the GPS observations in both the horizontal and vertical directions (Figure 8). The LAM predicts up to ~20 cm uplift on the eastern coast and ~10 cm subsidence in the inland areas in the first 2 years after the earthquake, which matches the overall pattern of the GPS observations well (Figure 8b). The slight systematic underestimate of the horizontal components along the eastern coast may be improved by including other structural processes, such as poroelastic rebound and relaxation of weakened lower crust beneath the volcanic arc of northeast Japan as reported in *Hu et al*. [2014]. The LAM does not predict the landward motion at the MYGI and KAMS seafloor sites. The near-field deformation in vicinities of the main rupture area strongly depends on

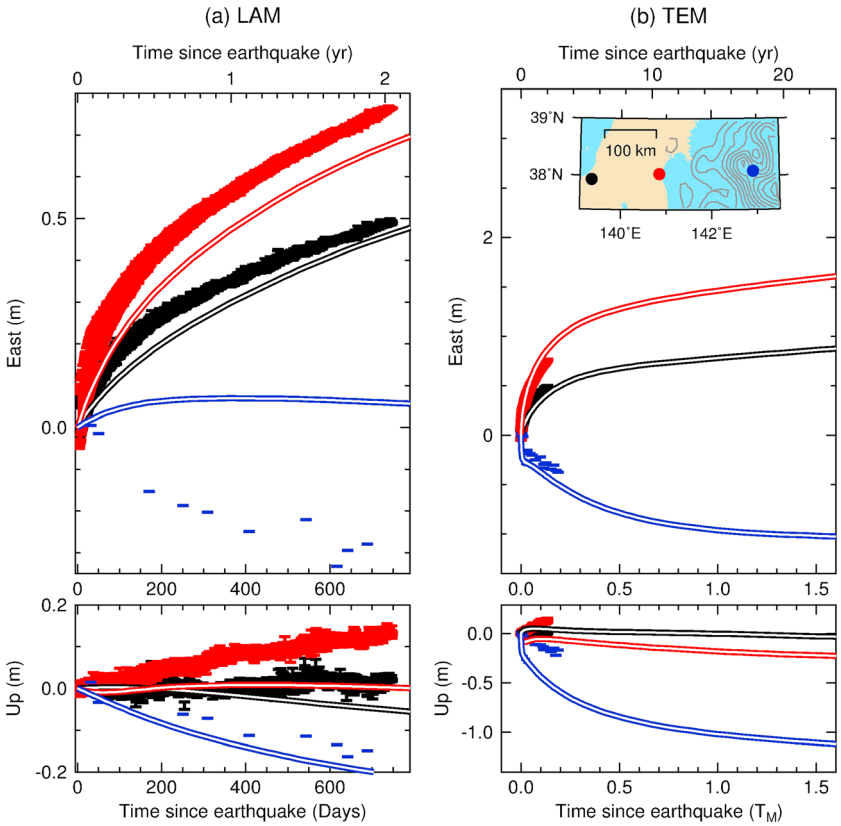


**Figure 9.** Observed postseismic-only displacement time series, compared with predicted motions from the LAM (see section 4.2) and TEM (see section 5.3), at three example surface points whose locations are illustrated in the inset in Figure 9b. The blue circle is GPS-A site MYGI in the peak slip area. Red and black circles are GEONET stations at the eastern and western coasts, respectively. Top and bottom images of the (a) LAM and (b) TEM are East and vertical displacements, respectively. $T_M = 15$ years is the characteristic Maxwell relaxation time of the mantle wedge. Color coding of data points and model lines in Figures 9a and 9b is the same as that of the stations in the map plot in Figure 9b.

the source model and distribution of the afterslip. If we allow local heterogeneities in the rheological structure and/or distribution of afterslip, for example, modifying the afterslip distribution by adjusting the locations of locked asperities or allowing viscosity heterogeneity in the shear zone, we could perfectly fit the GPS-A observations. However, the purpose of this paper is to understand the fundamental processes through studying the first-order pattern of the postseismic deformation. We thus do not make additional adjustments to fit individual stations.

The LAM does not predict the observed uplift south of the rupture area (lower left corner of Figure 8b). Horizontal fit in this region is also poorer than that near the main rupture area. This southern region is complicated by the subduction of the PSP and Boso slow slip sequences [*Ozawa*, 2014]. Our approach of removing the steady pre-earthquake deformation might also not be correct in this region, for example, it may be biased by other local processes, such as the 2000 eruption of the Miyakejima volcano [e.g., *Nakada et al.*, 2005] and slow slip events in the Tokai region, central Japan [e.g., *Hirose and Obara*, 2006]. In section 5.2, we will further examine the effects of the structural heterogeneity in this region on the postseismic deformation.

The LAM well reproduces the magnitudes and directions of very far-field GPS observations in China, Korea, Russia, and on the PSP, ~1000 to 2000 km from the 2011 rupture area (Figure 8c). Directions of two stations on the PAC are reproduced by the LAM, but their magnitudes are underestimated by a factor of ~3–5. The vertical components of these very far-field stations are not shown because of the negligible magnitude of the postseismic signal.

Figure 9a shows the comparison of the time series of three example stations 950172 (eastern coast), 940049 (western coast), and the GPS-A site MYGI with the LAM predicted displacements. The LAM fits well the overall

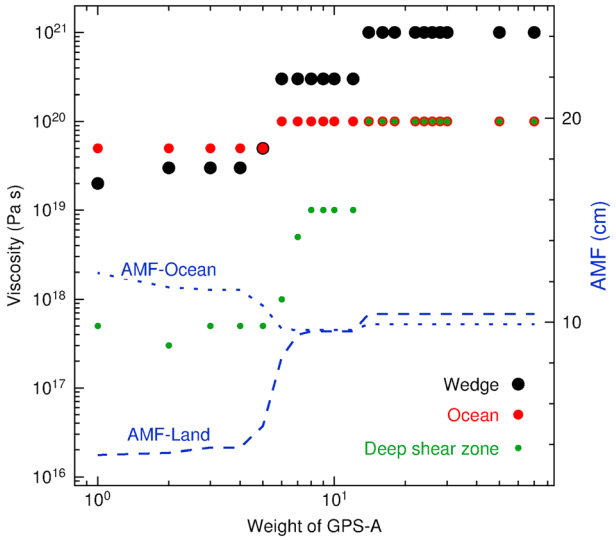


**Figure 10.** Effects of weights of the GPS-A on the preferred viscosities. Red, black, and green symbols are the preferred viscosities of the oceanic upper mantle, mantle wedge, and deep shear zone, respectively, at the corresponding weight of the GPS-A. Blue dashed and blue dotted lines represent the AMF of the GEONET (land GPS) and of the GPS-A (offshore) in the corresponding preferred model, respectively.

curvature of the time series of the GEONET and GPS-A stations. A constant underestimate of a few centimeters in the east component of 950172 and 940049 (top image in Figure 9a) may be due to 3-D structural heterogeneities (see discussion in section 5.1) or very rapid afterslip in the hours to a few days following the event [e.g., *Munekane*, 2012], which is not considered in this work. It is the fit to the curvature of the time series that determines how well the Burgers rheology represents the rapidly decaying postseismic deformation. The LAM well reproduces the observed subsidence of MYGI but fails to predict its horizontal landward motion (Figure 9a).

The LAM produces very rapid afterslip in the first 2 years after the earthquake. In the first half year following the 2011 earthquake the fault slips aseismically by up to ~2.8 m, with an aseismic moment equivalent to an earthquake of $M_w$8.2 (results not shown). Afterslip takes place mostly along the edges of the locked asperities (see discussion in section 3.2). Two years after the earthquake the cumulative slip of the fault is up to ~3.5 m. Distribution and evolution of the modeled afterslip in the shear zone will be discussed in more detail in section 5.3.

## 5. Discussion

After having studied the first-order pattern of postseismic crustal deformation in the preceding sections, we investigate possible roles of higher-order heterogeneities in rheological structure and subduction complexity. *Hu et al.* [2014] studied the potential contributions of poroelastic response of the shallow top layer in the continental and oceanic lithosphere and of a weakened, low-viscosity lower crust beneath the arc to the postseismic deformation. They have reported that poroelastic rebound is localized near the rupture zone. Their poroelastic models, using ranges of parameters based on previous studies [e.g., *Hughes et al.*, 2010], produced up to ~15 cm subsidence offshore, a zone of uplift at the updip edge of the rupture and up to ~30 cm landward motion offshore. Models in which the lower crust beneath the arc has a viscosity that is up to about one order of magnitude lower than the upper mantle wedge, produce up to ~20 cm seaward motion and ~15 cm uplift east of the arc, and up to ~10 cm seaward motion and ~20 cm subsidence west of the arc, in the first 2 years after the 2011 earthquake [*Hu et al.*, 2014]. These two processes can be parameterized to improve the fit of the LAM to the GPS measurements but involve a large number of additional free model parameters. In this section, we further consider the possible role of a weak asthenospheric layer underlying the oceanic lithosphere and explore the effects of the subduction of the Philippine Sea plate south of the Tohoku rupture zone. Then we report an updated model with the total effects (TEM) that is based on the LAM and includes the structural heterogeneities. Finally, we compare the combined contributions of the earthquake cycle deformation to the long-term coastal uplift.

### 5.1. Seafloor Geodetic Constraints on Oceanic Upper Mantle Rheology

In the test models shown in Figures 6a–6e and the LAM shown in Figure 8, there is a persistent large misfit at GPS-A stations. These models do not produce the observed magnitude of landward motion of the sites located above the high-slip zone (GPS-A stations, MYGI and KAMS) or of station G01 on the PAC. If we give more weight to the GPS-A in evaluating test models ($w$ in the second term of (1)); we obtain test models with a better fit to the GPS-A data. When $w \geq 6$, misfit to GPS-A is the lowest and varies only within 1 cm with an even larger $w$ (dotted blue lines in Figure 10). However, misfit to land GPS deteriorates dramatically if $w \geq 4$

(dashed blue lines in Figure 10). Although the viscosity of $\eta^O$ in models of $w \geq 6$ does not change much, the best fit $\eta^W$ and $\eta^S$ increase by more than one order of magnitude (Figure 10). The models that provide the best fit to the GPS-A stations suggest $\eta^O = 10^{20}$ Pa s, $\eta^W = 10^{21}$ Pa s, and $\eta^S = 10^{20}$ Pa s (Figure 6f). Higher viscosities in the mantle wedge and shear zone produce less seaward motion and thus lead to a better fit to these GPS-A stations. However, the fit to the land GPS observations deteriorates.

*Sun et al*. [2014] used a similar finite element model to study the landward motion of some of the GPS-A stations. They prescribed a kinematic motion of the fault to simulate the afterslip. In their model, displacements of the fault increase up to ~1.7 m in the first 5 years through a cubic function of time [*Hu and Wang*, 2012]. Their distribution of afterslip was based on *Ozawa et al*. [2012] and was modified to better fit the GPS data. Their assigned afterslip is generally smaller than that indicated by the repeating earthquakes and is about half of that derived in the LAM. Thus, they inferred much lower viscosities of the mantle wedge, with a steady state Maxwell viscosity $\eta_M = 1.8 \times 10^{18}$ Pa s and the transient Kelvin viscosity $\eta_K = 2.5 \times 10^{17}$ Pa s, about one order of magnitude lower than those of the LAM in this work, to compensate for the reduced seaward motions on land due to the underestimated afterslip. Deformation near the trench is less affected by the lower viscosities in the mantle wedge. Their model also features a low-viscosity lithosphere-asthenosphere boundary layer ($\eta_M = \eta_K = 2.5 \times 10^{17}$ Pa s). Viscosities of the oceanic upper mantle in their model are of the same order as that in the LAM. Because of generally smaller afterslip on the fault but faster relaxation of the oceanic side their model successfully reproduced the landward motion of MYGI and KAMS but failed to predict the postseismic deformation of the G01 on the Pacific plate [*Tomita et al*., 2015].

Allowing viscosity heterogeneity in the shear zone and/or modifying the geometry of the locked asperities presented in section 3.2 would improve the fit to the GPS observations, especially at the GPS-A stations. However, the main purpose of this paper is to understand the fundamental processes through studying the first-order pattern of the postseismic deformation. We do not introduce local heterogeneities to better fit individual stations. We do consider effects of other structural heterogeneities, for example, a weak suboceanic asthenospheric layer, that may help improve the fit to GPS observations.

The structure of the oceanic upper mantle has yet to be better understood. *Hu et al*. [2004] suggested that a higher viscosity in the oceanic upper mantle, for example, $10^{20}$ Pa s produces a better fit to the observed postseismic uplift along the coast after the 1960 $M_w$9.5 Chile earthquake. A low-velocity zone beneath the oceanic lithosphere, which may indicate a hydrated and weak asthenosphere, has been observed in seismic tomography profiles [e.g., *Kawakatsu et al*., 2009; *Obayashi et al*., 2009; *Li and van der Hilst*, 2010]. *Pollitz et al*. [1998] obtained a low viscosity $5 \times 10^{17}$ Pa s in the oceanic asthenosphere in a stress-triggering model of interplate earthquakes from 1952 to 1965 along the Aleutian arc and Kurile-Kamchatka trench. Deformation of GPS stations on land that are generally hundreds of kilometers away from the trench are subjected to the collective effects of the rheological structure of the oceanic upper mantle, and details of the depth-varying oceanic rheology profile are not resolvable. However, the near-field deformation, such as that at the GPS-A stations offshore, may be sensitive to variations in the rheological structure of the oceanic upper mantle. One of the best locations to study the oceanic upper mantle structure may be the Indian Ocean where the largest recorded $M_w$8.6 strike-slip earthquake occurred in 2012 [e.g., *Wei et al*., 2013].

If we included the thickness and viscosity of the asthenosphere into the model parameter space, the computing time would increase several fold and would be beyond our computing limit. Therefore, we initially use a uniform layer to average the total effects of the oceanic asthenosphere and upper mantle. In this section, we present a test model that includes an 80 km thick weak asthenosphere beneath the oceanic lithosphere, the same thickness of the oceanic lithosphere. The shear modulus and Poisson's ratio of the weak asthenosphere are the same as that of the upper mantle in the LAM. Other model parameters in the weak-asthenosphere model (WAS), such as the viscosities of the mantle wedge and oceanic upper mantle are the same as in the LAM. The model results presented in this section are calculated by differencing the outputs of the test model and the LAM.

If we assume the viscosity of the weak asthenosphere ($\eta^{AS}$) to be $10^{19}$ Pa s, one fifth of that of the oceanic upper mantle in the LAM, the effects of the asthenosphere produce up to ~20 cm landward motion near the trench, less than 20 cm uplift in a narrow zone along the trench, and up to ~15 cm of subsidence in the vicinity of the downdip edge of the main rupture zone (Figure 11a). Deformation on land is negligible, as expected. Near-field deformation scales with the viscosity of the asthenosphere. If we increase the

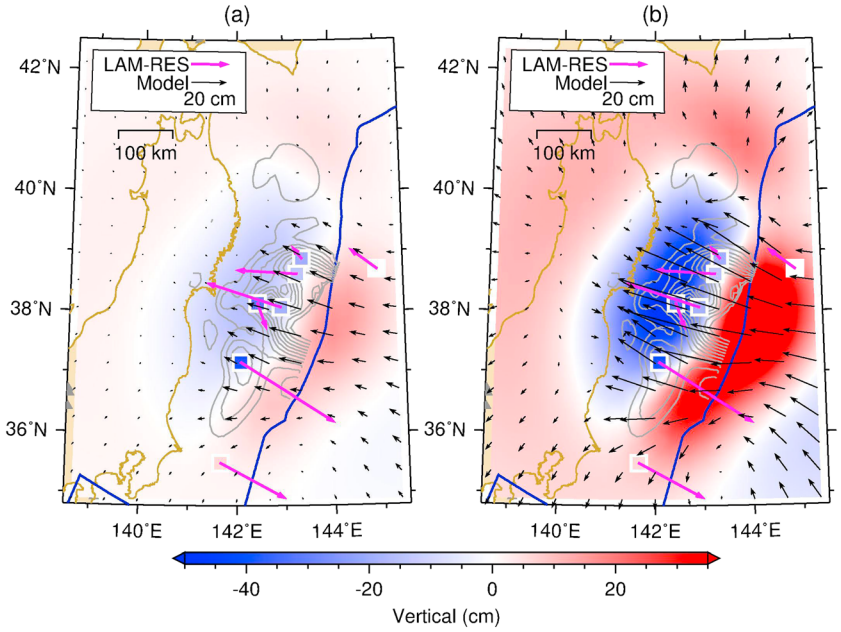


**Figure 11.** Effects of the viscoelastic relaxation in an 80 km thick weak asthenosphere beneath the oceanic lithosphere on the surface deformation. Black arrows and color contours represent modeled horizontal and vertical surface postseismic deformation in the first 2 years after the earthquake, respectively. Magenta arrows and filled white rectangles represent the horizontal and vertical residuals of GPS-A stations in the LAM as shown in Figure 8. The color scale of the vertical components of the misfit and model predictions is the same. The viscosity of the asthenosphere is (a) $10^{19}$ Pa s and (b) $10^{18}$ Pa s. The viscosity of the oceanic upper mantle is $5 \times 10^{19}$ Pa s in Figure 11a and $10^{20}$ Pa s in Figure 11b.

viscosity of the oceanic upper mantle by a factor of 2 ($10^{20}$ Pa s) and decrease that of the asthenosphere by a factor of 10 ($10^{18}$ Pa s) (Figure 11b), the WAS produces up to ~60 cm landward motion and up to ~30 cm subsidence above the downdip edge of the rupture zone (Figure 11b). Figure 11 indicates that an asthenosphere viscosity of at least $10^{18}$ Pa s is able to produce enough landward motion at MYGI in the forearc and at G01 on the PAC to match the observed displacements. Given the limited data constraints, a systematic analysis of the thickness and viscosity of the oceanic asthenosphere is beyond the focus of this work. We hope to further illuminate this question in a study of the postseismic deformation of the 2012 $M_w$8.6 Indian Ocean earthquake.

### 5.2. Effects of the Subducting Philippine Sea Plate

Comparison of GPS observations with predicted displacements in the LAM as shown in Figure 8 indicates a persistent underestimate of the GPS displacements south of the rupture zone, the triple junction area where the PSP subducts beneath the OKT and the PAC subducts beneath the PSP. The magnitude of the misfit is small compared to the postseismic signal over most of Japan, but misfits reach more than 10 cm in the south, where the PSP subducts.

Building on the LAM, we have constructed test models that include the subduction of the PSP to study the effects of this rheological heterogeneity on the viscoelastic postseismic deformation following the 2011 earthquake. The geometry of the subduction interface of the PSP (green dashed lines in Figure 12) is based on *Uchida et al.* [2010b]. We assume that the elastic thickness of the PSP is 30 km because of the young age of the PSP [e.g., *Hall et al.*, 1995]. Varying the PSP thickness by up to a couple of tens of kilometers produces negligible changes on the surface deformation. The viscosity of the mantle wedge shaped by the PSP and overlying OKT is the same, $3 \times 10^{19}$ Pa s, as that of the mantle wedge formed by OKT and PAC in the LAM. The viscosity of the oceanic upper mantle beneath the PSP is the same, $5 \times 10^{19}$ Pa s, as that of the oceanic upper mantle beneath the PAC in the LAM. Similar to section 5.1, the model results in this section are calculated by differencing the output of test models and the LAM such that the obtained results are only due to the effects of the introduction of the subducting PSP.

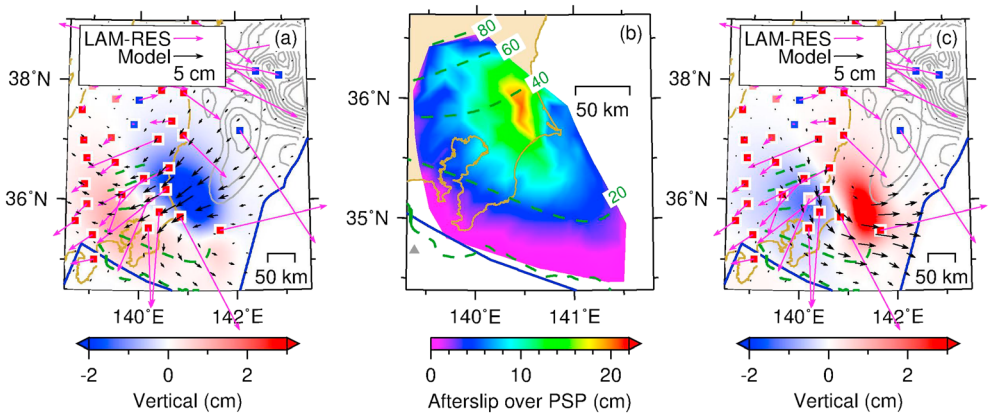


**Figure 12.** Effects of the elastic subducting Philippine Sea plate (PSP) and afterslip on the PSP-OKT plate interface on the surface deformation. (a) Surface displacements 2 years after the earthquake only due to the elastic PSP slab. Similar to Figure 11, black arrows and color contours represent horizontal and vertical model displacement components, respectively. Magenta arrows and filled white squares represent the spatially downsampled horizontal and vertical residuals of GPS observations in the LAM as shown in Figure 8. Thick green dashed lines represent the depth contours (labeled in Figure 12b) on the top of the PSP slab [*Uchida et al.*, 2010b]. Thick blue solid lines represent the location of the trench. (b) Modeled amplitude of afterslip on the PSP-OKT plate boundary with a viscosity $10^{19}$ Pa s in the shear zone. (c) Surface deformation in the first 2 years after the earthquake only due to the PSP-OKT afterslip shown in Figure 12b.

The elastic subducting PSP slab acts as a barrier to block the northeast viscoelastic material flow in the mantle wedge induced by the 2011 earthquake. The net effect of this barrier is to cause areas east of the barrier to move southwest and downward (subsidence) and to cause areas west of the barrier to move northeast and upward (uplift) (Figure 12a). The hinge line of the surface uplift and subsidence, with peak values of ± ~2 cm, approximately aligns with the downdip edge of the subducting PSP slab. The overall southwest motion and uplift produced by introducing the PSP improves the fit to the GPS observations. However, the ~4 cm horizontal motion does not suffice to account for the up to ~20 cm misfit of the LAM in this region (Figure 12a). The uplift above the PSP improves the fit to the GPS observations.

Repeating earthquakes indicate that the subducting PSP slab slipped aseismically below the OKT by up to 23 cm in the first 700 days after the 2011 earthquake (see section 2.3). Afterslip over segments of the subducting PAC slab beneath the PSP in this region is less than 15 cm based on repeating earthquakes (results not shown) and has already been accounted for by a weak shear zone over the PAC (see discussion in section 3.2). Taking the same approach of introducing a weak shear zone as applied to the PAC, we construct a weak shear zone along the subducting PSP slab to study the effects of the stress-driven afterslip of the PSP. We use a thickness of 20 km in the PSP shear zone because of the coarse element size in this region. We use a trial-and-error approach to determine the viscosity of the shear zone of the PSP. For simplicity, we use a uniform viscosity in the whole weak shear zone. When the viscosity of the shear zone is $10^{19}$ Pa s, the modeled afterslip of the PSP is on the order of ~15 cm, consistent with that indicated by the repeating earthquakes (Figure 12b). The unit thickness viscosity of the PSP slab is $5 \times 10^{17}$ Pa s/km, about the same order as that of the PAC in the LAM. Afterslip of the PSP produces up to ~3 cm uplift east of the PSP which improves the fit of the LAM to GPS and up to ~2 cm subsidence above the PSP that degrades the fit to GPS in the LAM in this region (Figure 12c). The clockwise rotation of the surface deformation from the modeled afterslip of up to ~4 cm does not help to reduce the misfit indicated by the southwesterly horizontal residual motion of up to ~20 cm. Note that the model results shown in Figure 12c are the contribution from the afterslip of the PSP as well as the existence of the subduction PSP slab.

The above tests indicate that introducing the subduction and afterslip of the PSP can modestly improve the fit to the GPS data, but they do not suffice to reduce the whole misfit in the LAM (Figure 12). The removed pre-earthquake trends in this region described in section 2.1 may be biased by effects of the 2000 eruption of the Miyakejima volcano [e.g., *Nakada et al.*, 2005] and slow slip events in the Tokai region, central Japan [e.g., *Hirose and Obara*, 2006]. There might be other processes that contributed to the postseismic surface deformation of the 2011 earthquake. For example, (1) *Ozawa* [2014] reported that the recurrence interval of Boso slow slip sequences in this region decreased from 6.4 years before the 2011 earthquake to 2.2 years

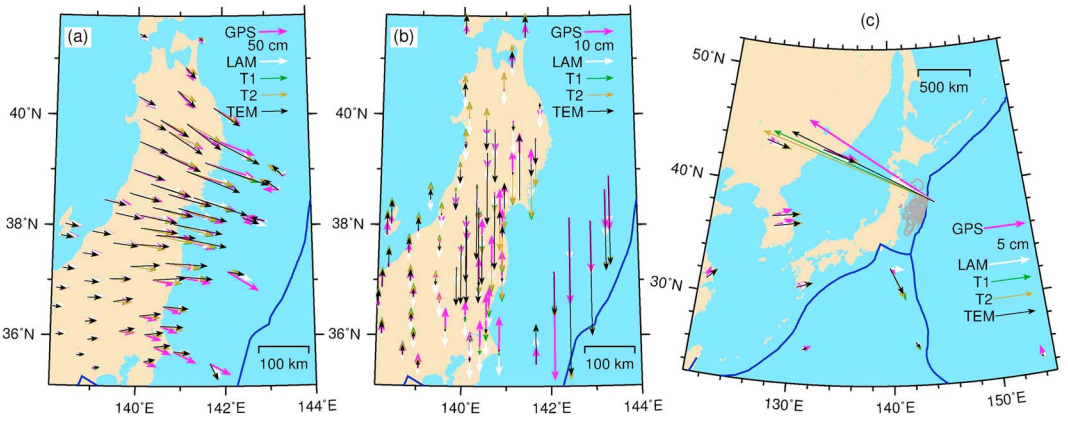


**Figure 13.** Comparison of 2 years postseismic GPS observations at quadtree-selected stations with model-predicted displacements. (a) Horizontal displacements. (b) Vertical displacements. (c) Comparison of very far-field GPS observations with model-predicted displacements. Magenta and white arrows represent GPS observations and model-predicted displacements in the LAM, respectively. Structural heterogeneities, the oceanic asthenosphere (OASP), subduction PSP (SPSP), and weakened lower crust beneath the arc (WLCA) are incorporated into the LAM step by step, that is, T1 = LAM + OASP, T2 = T1 + SPSP, and TEM = T2 + WLCA.

after the earthquake. *Ozawa* [2014] reported that the equivalent moment magnitude of the recent slow slip event from approximately 28 December 2013 to 10 January 2014 is ~6.5. Accounting for the slow slip events would produce more seaward motion in this region and may reduce the misfit of the LAM. (2) The PSP may not only act as a barrier to block viscoelastic postseismic material flow as discussed above but may also weaken the above mantle wedge through the dehydration of the hydrated subduction PSP slab. A model of a weaker mantle wedge shaped between the PSP and OKT would likely produce larger surface deformation (as illustrated in Figure 4a). For the purposes of this paper we do not attempt to explicitly pursue these additional model complexities.

### 5.3. Future Predictions of Total Effects Model (TEM)

In this section, we construct a test model of total effects of the rheological elements described in the LAM as well as structural heterogeneities investigated in the preceding sections and in *Hu et al.* [2014]. On the basis of the LAM, we construct two transitional test models in order to account for these heterogeneities step by step (Figure 13). First, we include an 80 km thick oceanic asthenosphere (OASP) into the LAM, that is, a test model T1 = LAM + OASP. Viscosities of the asthenosphere and the underlying oceanic upper mantle are $10^{18}$ Pa s and $10^{20}$ Pa s, respectively (see section 5.1). The OASP greatly improves the fit to the GPS-A stations offshore and two stations on the PAC. Fit to the vertical component of the far-field GPS observations on land is also improved. From T1 we then account for the effects of subduction and afterslip of the PSP (SPSP) (see section 5.2), that is, $T2 = T1 + \mathrm{SPSP}$. The SPSP results in a change in the 2 year postseismic surface deformation of less than a few centimeters. Finally, we account for a weakened lower crust beneath the arc (WLCA) described in *Hu et al.* [2014], that is, $\mathrm{TEM} = T2 + \mathrm{WLCA}$. Following *Hu et al.* [2014], the rheology structure of the WLCA in this work is as follows: the viscosity of the weakened lower crust decreases linearly with depth from $10^{23}$ Pa s to $10^{18}$ Pa s between depths of 15 km and 25 km. At depths greater than 25 km, the viscosity is fixed at $10^{18}$ Pa s. The bottom of this lower viscosity zone is set to be at the depth of 100 km, approximately extending up to the subduction interface. However, the surface deformation is not sensitive to the bottom depth as long as it is at least a couple of tens of kilometers greater than the continental lithospheric thickness (40 km). The plain-view width of the weakened zone is 50 km. The pattern of the 2 year postseismic surface deformation produced by the WLCA is an overall seaward displacement of up to ~30 cm, an uplift of up to ~20 cm in areas east of the arc, and a subsidence of up to ~30 cm in areas west of the arc.

The TEM predicts that the viscoelastic postseismic deformation of the 2011 earthquake will continue for hundreds of years although the deformation slows dramatically with time after about 5 years (Figure 9b). The long-lasting postseismic deformation of the Tohoku earthquake is consistent with studies of the subduction-zone earthquake cycle deformation in other margins [e.g., *Suito and Freymueller*, 2009;

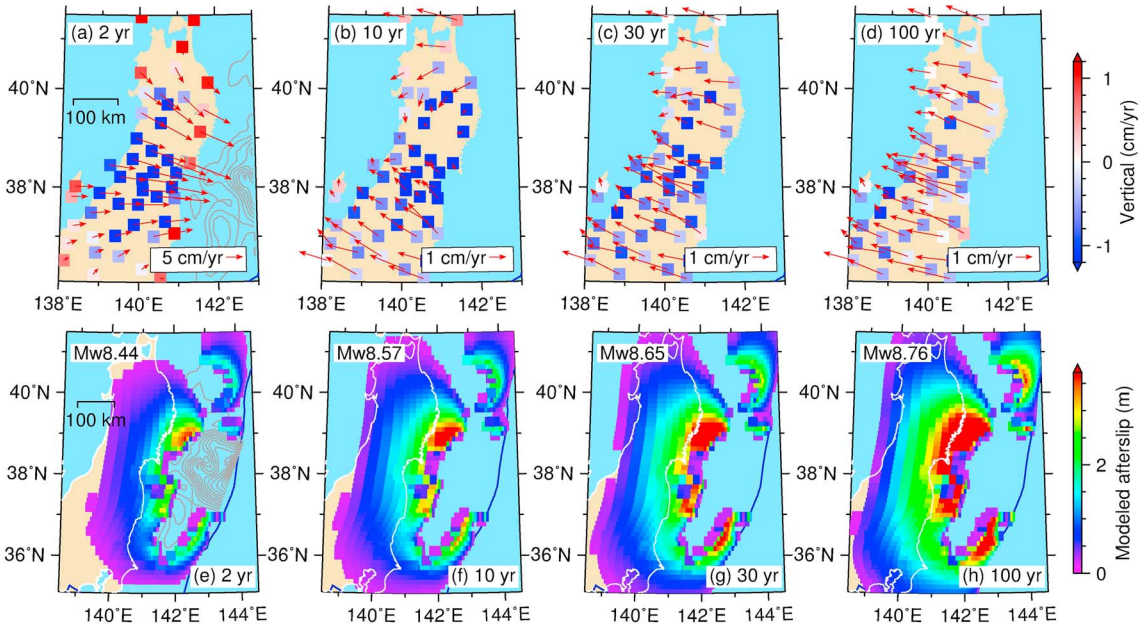


**Figure 14.** Model-predicted surface velocities including postseismic deformation of the 2011 earthquake as well as the steady plate convergence and modeled afterslip at different times. Surface velocities are plotted at (a) 2, (b) 10, (c) 30, and (d) 100 years after the 2011 event. Red arrows and color contours represent horizontal and vertical components, respectively. Modeled aseismic slip in the shear zone is plotted at (e) 2, (f) 10, (g) 30, and (h) 100 years after the 2011 event. Equivalent moment magnitude of the modeled afterslip for each plot is labeled in the insert text.

*Wang et al*., 2012]. We have described the individual contributions of the three rheological elements to the surface deformation in section 4.1. For example, the oceanic upper mantle produces overall landward motion and subsidence in the upper plate, while the mantle wedge results in overall seaward motion and uplift. Because the characteristic relaxation times of the three rheological elements are different, the combined effects may result in temporary reversals in the sign of the surface deformation. For example, the uplift of the two coastal sites (red and black lines in the bottom image of Figure 9b) are expected to reverse within about 2 years after the earthquake.

Predicted motions of the GPS stations in future years may be obtained through the model-predicted surface deformation superimposed on the long-term linear trend that was removed earlier (see discussion in section 2.1). This approach assumes that the interseismic velocities are steady over the time period of model predictions, but a modest acceleration of ~1 mm/yr$^2$ in the interseismic velocities during 1996–2010 was reported by *Mavrommatis et al*. [2014]. The TEM predicts that an opposing motion of the land area, that is, landward motion on the eastern coast and seaward motion on the western coast, will be observed starting about 10 years after the earthquake (Figure 14b). Such opposing motion is presently observed in Chile [*Wang et al*., 2007] and Alaska [*Suito and Freymueller*, 2009], where previous megathrust earthquakes occurred decades ago. Thirty years after the earthquake, the whole land area is predicted to move landward although the velocities of the western coast will be lower than those observed before the earthquake (Figure 14c). The shorter time span of the opposing motion in NE Japan compared to Alaska [*Suito and Freymueller*, 2009] and Chile [*Hu et al*., 2004] is probably due to the shorter along-strike length of the 2011 earthquake [*Hu et al*., 2004]. After ~100 years the surface deformation will be controlled mainly by the steady plate convergence (Figure 14d). GPS stations along the eastern coast will move toward land at velocities approximately the same as seen before the earthquake, a scenario that is presently observed in Cascadia where the 1700 $M_w$9.0 earthquake occurred [*McCaffrey et al*., 2013].

The modeled afterslip in the weak shear zone following the 2011 earthquake decays rapidly with time (Figures 14e–14h). In the first 2 years after the earthquake the equivalent moment magnitude of the modeled afterslip is $M_w$8.44 (Figure 14e). It will take the next 28 years to double the equivalent moment of the modeled afterslip (Figure 14g). After ~30 years, the distribution and magnitude of the cumulative afterslip is not expected to change much with increasing time, because the rate of slip will be nearly zero (Figure 14g).

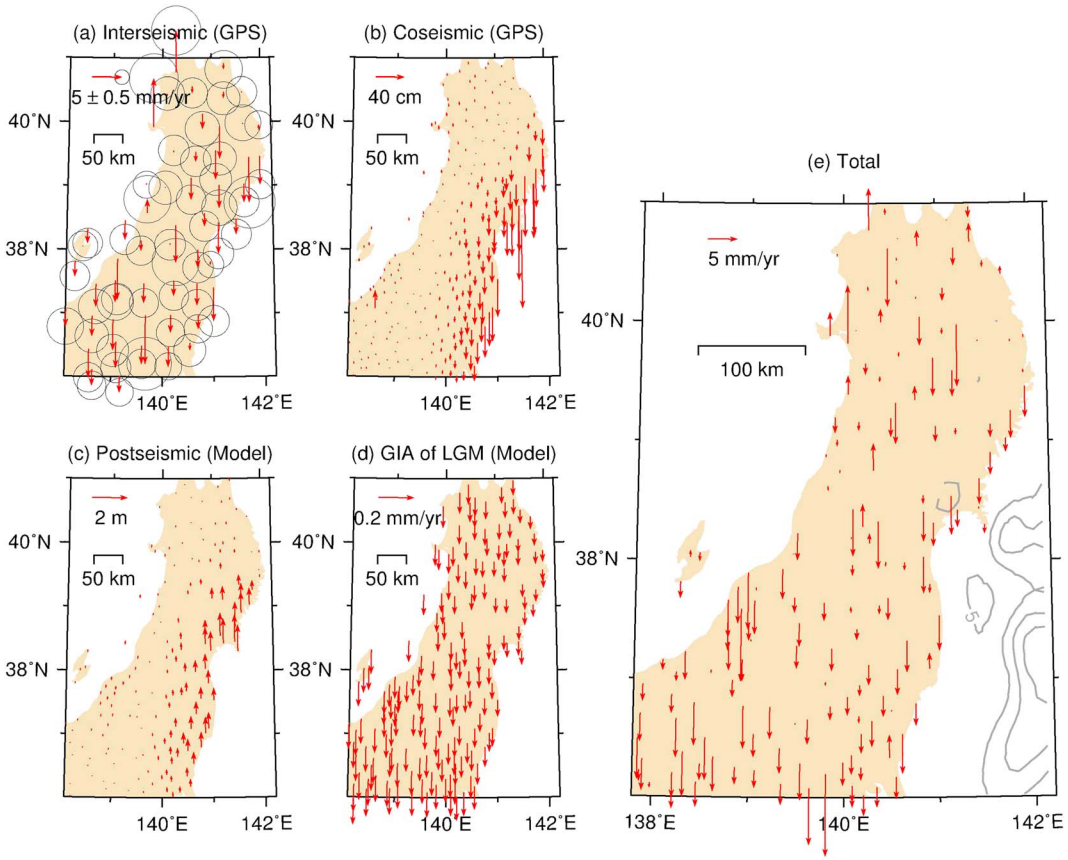


**Figure 15.** Vertical deformation through the earthquake cycle of NE Japan. (a) Interseismic vertical velocities at GPS stations averaged from 1998 to 2002. GPS stations are spatially downsampled to improve the legibility of observation uncertainties. The total effects in Figure 15e are still calculated over the original unsampled data. (b) Coseismic vertical displacements observed at GPS stations. (c) Total postseismic displacements modeled by the TEM after complete relaxation. (d) Present vertical deformation rate due to a model of glacial isostatic adjustments (GIA) of the last glacial maximum (LGM) [*Spada*, 2003]. (e) Total effects of Figures 15a–15d for estimate of long-term vertical motion of NE Japan.

After 100 years, the predicted annual moment release by afterslip is ~$5.2 \times 10^{19}$ N m/a ($M_w$7.1), and the equivalent moment magnitude of the modeled afterslip is 8.76, about 36% of the total moment of the main shock (Figure 14h).

### 5.4. Reconciling Long-Term Coastal Uplift With Earthquake Cycle Deformation

There is a long-standing debate regarding the observed pattern of vertical deformation indicating interseismic and coseismic subsidence that appear to be in conflict with the long-term terrace uplift along the northeastern coast of Japan [e.g., *Heki*, 2007]. For example, late Quaternary marine terraces indicate slow long-term uplift of 0.1–0.4 mm/yr along the Pacific coast [e.g., *Koike and Machida*, 2001; *Ota and Yamaguchi*, 2004; *Matsu'ura et al.*, 2009]. However, tide gauge data in this region indicate subsidence rates of ~5 mm/yr averaged over 1966–1999 [*El-Fiky and Kato*, 1999] and of ~1–16 mm/yr averaged over 1951–1981 [*Kato*, 1983]. In both papers coseismic and postseismic vertical deformation of several *M*7 earthquakes were considered to be short-time lived and were not corrected for deriving the secular vertical rate. The GPS time series of GEONET over the last couple of decades indicate intermediate subsidence rates of ~1–5 mm/yr in NE Japan (Figure 15a), and this region also subsided coseismically. *Suwa et al.* [2006] referenced their GPS data to a station at the western coast (38.5°N and 139.5°E) and obtained up to ~5 mm/yr subsidence at the eastern coast by averaging GPS time series from 1997 to 2001. The magnitude of their obtained subsidence is similar to that of this work shown in Figure 15a. *Aoki and Scholz* [2003] referenced their GPS data to a station near the Pacific coast at the latitude 36.11°N and longitude 140.09°E and reported no significant vertical deformation along the Pacific coast by averaging GPS time series from 1996 to 1999.

Nevertheless, how can a region that shows long-term uplift subside both in the interseismic and coseismic parts of the earthquake cycle? *Sagiya* [2015] used a two-layered model, that is, 40 km elastic lithosphere overlying viscoelastic upper mantle, to simulate repeated occurrences of megathrust earthquakes as well as the plate convergence motion and to obtain the net vertical surface deformation over many earthquake cycles. He concluded that shallow great earthquakes with recurrence interval of a few hundred years may be responsible for the long-term coast uplift. In this section, we discuss if the slow long-term coastal uplift may be reconciled by considering earthquake cycle deformation including the postseismic period. We study the surface deformation due to processes of interseismically relocking of the fault, coseismic rupture, viscoelastic postseismic deformation, and glacial isostatic rebound since the last glacial maximum (LGM). Other potential processes include continuous accretion or erosion of subducted sediments beneath the continental upper plate [e.g., *Heki*, 2004; *Clift and Vannucchi*, 2004; *von Huene et al*., 2004; *Uchida et al*., 2010a], erosion and transportation of surface material, and spreading of the back arc [e.g., *Kimura and Tamaki*, 1986]. These processes either produce only secondary-order contributions to the coast surface deformation or are limited by lack of observations and are not examined in this work.

We first estimate the effect of glacial isostatic rebound since the LGM on present surface deformation. For simplicity, we use the ICE-3G model that is included in TABOO [*Spada*, 2003]. We use an Earth model that includes a 120 km elastic lithosphere overlying three layers of viscoelastic upper mantle separated at depths of 400 km and 670 km. The viscosity of the three layers are $10^{21}$, $10^{21}$, and $2 \times 10^{21}$ Pa s from top to bottom which is the same as in VM1 [*Argus and Peltier*, 2010]. GIA of LGM produces a negligible subsidence rate ~0.1 mm/yr in NE Japan (Figure 15d). Using recent GIA models such as ICE-6G (VM5a) [*Toscano et al*., 2011] will not change the fundamental pattern of the surface subsidence because NE Japan is far from the unloading center of LGM.

The interseismic deformation which is removed to derive postseismic displacements as shown in Figure 1 is calculated from GPS time series during 1998–2002. Most GPS stations underwent ~1–5 mm/yr subsidence during that period (Figure 15a). The last giant earthquake prior to the 2011 event may be the 869 Jōgan earthquake [*Minoura et al*., 2001; *Sawai et al*., 2008]. The recurrence interval for *M*9 earthquakes in NE Japan may be 500–800 years [e.g., *Weldon et al*., 2004; *Sawai et al*., 2012]. The total subsidence in an earthquake cycle due to relocking of the fault is thus ~0.54 m. The 2011 event produced up to more than 40 cm coseismic subsidence along the Pacific coast (Figure 15b). In contrast, the cumulative viscoelastic postseismic deformation due to the 2011 event is predicted to produce up to ~2 m of uplift along the Pacific coast in the LAM (Figure 15c).

The combined effects over one earthquake cycle of $\leq$2 m postseismic uplift of the 2011 earthquake, $\leq$0.4 m coseismic subsidence from the 2011 earthquake, ~0.5–4 m interseismic subsidence derived from GPS time series, and ~0.1 m subsidence from GIA result in up to ~3 mm/yr subsidence along the Pacific coast, which is contrary to the observed long-term uplift of marine terraces (Figure 15e).

The observed interseismic deformation in a short time interval of the GPS data (Figure 15a) may not be representative of the long-term interseismic deformation that includes contributions of small earthquakes and slow slip events. *Mavrommatis et al*. [2014] also reported ~1 mm/yr$^2$ acceleration in the interseismic velocities during 1996–2010. Thus, we use an alternative approach to estimate another scenario of interseismic slip and coastal uplift.

We assume that the locked portions of the megathrust are outlined by the 10 m coseismic rupture contour lines [*Iinuma et al*., 2012]. We then kinematically prescribe the megathrust at a uniform fixed subduction rate 8 cm/yr [*Altamimi et al*., 2011]. It would take at least 600 years to accumulate enough strain for earthquakes such as the 2011 event. The modeled horizontal surface velocities agree well with the GPS observations (results not shown). For the vertical component, the model produces up to ~4 mm/yr uplift in a narrow eastern coast area and ~2 mm/yr subsidence in a broad inland area (Figure 16a). Replacing the interseismic effects shown in Figure 15a with those shown in Figure 16a, the total effects thus result in up to ~2 mm/yr uplift along the Pacific coast, which is more consistent with geological terrace uplift. We suggest that the interseismic velocities derived from GPS observations were not proportionately represented in the last century, perhaps because of the late stage of the earthquake cycle for the megathrust. In either case, the viscoelastic postseismic deformation appears to be one of the primary processes contributing to the long-term terrace uplift along the coast.

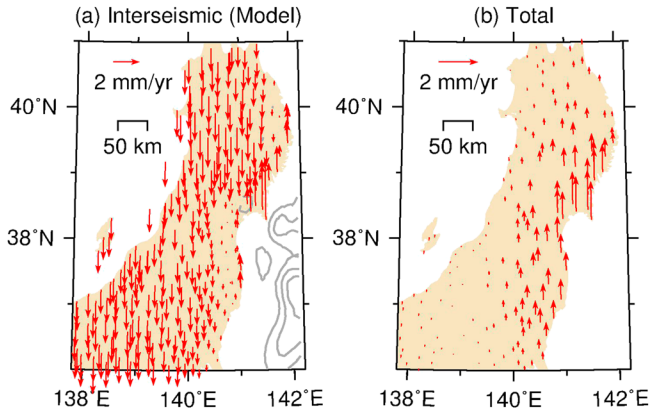


**Figure 16.** Alternative model-predicted interseismic vertical velocities and the net effects of vertical deformation in earthquake cycles. (a) Modeled interseismic vertical deformation by assuming that the released strain of the 2011 earthquake was accumulated linearly with time in the last 600 years. (b) Total effects of Figures 16a and 15b–15d.

## 6. Conclusions

We have constructed a 3-D viscoelastic finite element model to study the postseismic deformation of the 2011 $M_w$9.0 Tohoku-Oki earthquake. We apply a 2 km thick weak shear zone attached to the fault to model the stress-driven, time-dependent afterslip on the fault. The viscosity of the shear zone at the seismogenic depths (≤50 km) is determined to be $10^{17}$ Pa s from repeating earthquakes. We carried out systematic tests on the viscosities of the shear zone at greater depths, continental mantle wedge, and oceanic upper mantle. We evaluated hundreds of test models through comparison of continuous GEONET stations on land, far-field IGS stations, and campaign-mode GPS-A stations offshore with model-predicted displacements. Viscosities of the deep shear zone, mantle wedge, and oceanic upper mantle are determined to be $5\times10^{17}$ Pa s, $3\times10^{19}$ Pa s, and $5\times10^{19}$ Pa s, respectively, in our lowest averaged-misfit model (LAM). The order of the obtained viscosities in the mantle wedge and oceanic upper mantle is consistent with previous studies of other subduction zones, such as Cascadia [*Wang et al*., 2012], Chile [*Hu et al*., 2004], Alaska [*Suito and Freymueller*, 2009], and Sumatra [*Hu and Wang*, 2012]. The LAM fits well the first-order pattern of GPS observations on land and offshore both in horizontal and in vertical directions.

We modeled the effects of the individual rheological elements on the viscoelastic postseismic crustal deformation. The viscoelastic relaxation of the mantle wedge produces seaward motion and uplift in the upper plate, a reversed pattern to that of the oceanic upper mantle. Viscoelastic deformation due to afterslip depends highly on the distribution and magnitude of the afterslip. Afterslip produces overall seaward motion above, uplift updip of the afterslip zone and subsidence downdip. Observed surface deformation is a combination of the interplay of these three processes.

Tests on the heterogeneity of the rheology indicate that subduction of the Philippine Sea plate (PSP) and afterslip of the PSP produces viscoelastic surface deformation in the first 2 years after the 2011 earthquake of a few centimeters. An 80 km thick weak asthenosphere beneath the oceanic lithosphere produces surface deformation mostly near the trench of which the pattern is landward motion offshore, uplift within a few tens of kilometers from the trench, subsidence in the vicinities of the downdip edges of the rupture area, and uplift farther inland. A weak asthenosphere with a low viscosity of at least $10^{18}$ Pa s may suffice to produce enough landward motion at the GPS-A stations.

Building on the LAM, we integrate effects of 3-D structural heterogeneities into a preferred model with total effects (TEM) that include the oceanic asthenosphere ($10^{18}$ Pa s) overlying the oceanic upper mantle ($10^{20}$ Pa s), subduction and afterslip of the PSP, and a 50 km wide weakened lower crust ($10^{18}$ Pa s) beneath the arc. TEM successfully reproduces the landward motion of GPS-A stations offshore and improves the fit to the vertical GPS observations in the far-field more than 300 km from the rupture area. At least about 10 years after the earthquake, the TEM predicts an opposing motion on land. After about 100 years, earthquake-induced stresses in the upper mantle will be mostly relaxed and all the GPS stations are predicted to move landward. Modeled afterslip in the shear zone decays rapidly with time and is up to ~3.5 m in the first 2 years after the earthquake, equivalent to an earthquake of moment magnitude 8.44. After ~100 years the equivalent moment magnitude is 8.76, about 36% the moment of the main shock.

We also study how the earthquake cycle deformation reported in this work may reconcile the long-term coastal uplift. We study the combined surface deformation in the coastal area in one earthquake cycle due to processes of interseismically relocking of the fault, coseismic rupture (≤0.4 m subsidence), viscoelastic

postseismic deformation (≤2 m uplift), and glacial isostatic rebound since the last glacial maximum (~0.1 m). If the interseismic deformation due to the relocking of the fault is averaged from GPS time series, that is, ~0.5–4 m subsidence in one earthquake cycle, the net coast deformation of the total effects is ~3 mm/yr subsidence which is contrary to the observed long-term uplift of marine terraces. We construct a model of interseismic relocking of the fault in which the strain released in the 2011 event accumulates linearly with time in 600 years. If the interseismic deformation is calculated from the model and is ~2.4 m uplift in one earthquake cycle, the net coast deformation is ~2 mm/yr uplift which is more consistent with geological terrace uplift.

**Acknowledgments**

GPS daily time series recorded at the GEONET and IGS stations are from Geospatial Information Authority of Japan (http://datahouse1.gsi.go.jp/terras/terras_english.html) and Nevada Geodetic Laboratory (http://geodesy.unr.edu/index.php), respectively. Derived postseismic GPS displacements and model results for this paper are available by contacting Y.H. at yhu@seismo.berkeley.edu. The data of repeating earthquakes are available by contacting N.U. at naoki.uchida.b6@tohoku.ac.jp. We thank Bruce Buffett for providing the computing facility and thank GSI for the publicly available GPS time series of GEONET. We thank Laura Wallace, Sylvain Barbot, and another anonymous reviewer for thoughtful comments that improved the manuscript. This work was funded by NSF award EAR-1246850 and benefitted from support by the Miller Institute for Basic Research in Science. J.F. was funded by NSF award EAR-1246927. Berkeley Seismological Laboratory contribution 16-1.

## References

Altamimi, Z., X. Collilieux, J. Legrand, B. Garayt, and C. Boucher (2007), ITRF2005: A new release of the International terrestrial reference frame based on time series of station positions and Earth orientation parameters, *J. Geophys. Res.*, *112*, B09401, doi:10.1029/2007JB004949.

Altamimi, Z., X. Collilieux, and L. Métivier (2011), ITRF2008: An improved solution of the international terrestrial reference frame, *J. Geod.*, *85*, 457–473, doi:10.1007/s00190-011-0444-4.

Aoki, Y., and C.H. Scholz (2003), Vertical deformation of the Japanese islands, 1996–1999, *J. Geophys. Res.*, *108*(B5), 2257, doi:10.1029/2002JB002129.

Argus, D. F., and W. R. Peltier (2010), Constraining models of postglacial rebound using space geodesy: A detailed assessment of model ICE-5G (VM2) and its relatives, *Geophys. J. Int.*, *181*, 697–723, doi:10.1111/j.1365-246X.2010.04562.x.

Barbot, S., Y. Fialko, and Y. Bock (2009), Postseismic deformation due to the $M_w$ 6.0 2004 Parkfield earthquake: Stress-driven creep on a fault with spatially variable rate-and-state friction parameters, *J. Geophys. Res.*, *114*, B07405, doi:10.1029/2008JB005748.

Bedford, J., et al. (2013), A high-resolution, time-variable afterslip model for the 2010 Maule $M_w$ = 8.8, Chile megathrust earthquake, *Earth Planet. Sci. Lett.*, *383*, 26–36, doi:10.1016/j.epsl.2013.09.020.

Bird, P. (2003), An updated digital model of plate boundaries, *Geochem. Geophys. Geosyst.*, *4*(3), 1027, doi:10.1029/2001GC000252.

Broerse, T., R. Riva, W. Simons, R. Govers, and B. Vermeersen (2015), Postseismic GRACE and GPS observations indicate a rheology contrast above and below the Sumatra slab, *J. Geophys. Res. Solid Earth*, *120*, 5343–5361, doi:10.1002/2015JB011951.

Bürgmann, R., and G. Dresen (2008), Rheology of the lower crust and upper mantle: Evidence from rock mechanics, geodesy, and field observations, *Annu. Rev. Earth Planet. Sci.*, *36*, 531–567, doi:10.1146/annurev.earth.36.031207.124326.

Chopra, P. N. (1997), High-temperature transient creep in olivine rocks, *Tectonophysics*, *279*, 93–111.

Clift, P., and P. Vannucchi (2004), Controls on tectonic accretion versus erosion in subduction zones: Implications for the origin and recycling of the continental crust, *Rev. Geophys.*, *42*, RG2001, doi:10.1029/2003RG000127.

Diao, F., X. Xiong, R. Wang, Y. Zheng, T. R. Walter, H. Weng, and J. Li (2014), Overlapping post-seismic deformation processes: Afterslip and viscoelastic relaxation following the 2011 $M_w$ 9.0 Tohoku (Japan) earthquake, *Geophys. J. Int.*, *196*, 218–229, doi:10.1093/gji/ggt376.

Dieterich, J. H. (1994), A constitutive law for rate of earthquake production and its application to earthquake clustering, *J. Geophys. Res.*, *99*, 2601–2618, doi:10.1029/93JB02581.

El-Fiky, G. S., and T. Kato (1999), Interplate coupling in the Tohoku district, Japan, deduced from geodetic data inversion, *J. Geophys. Res.*, *104*, 20,361–20,377, doi:10.1029/1999JB900202.

Engdahl, E. R., R. van der Hilst, and R. Buland (1998), Global teleseismic earthquake relocation with improved travel times and procedures for depth determination, *Bull. Seismol. Soc. Am.*, *88*(3), 722–743.

Freed, A. M., and R. Bürgmann (2004), Evidence of power law flow in the Mojave desert mantle, *Nature*, *430*, 548–551, doi:10.1038/nature02784.

Freed, A. M., R. Bürgmann, E. Calais, J. Freymueller, and S. Hreinsdóttir (2006), Implications of deformation following the 2002 Denali, Alaska, earthquake for postseismic relaxation processes and lithospheric rheology, *J. Geophys. Res.*, *111*, B01401, doi:10.1029/2005JB003894.

Freed, A. M., T. Herring, and R. Bürgmann (2010), Steady-state laboratory flow laws alone fail to explain postseismic observations, *Earth Planet. Sci. Lett.*, *300*, 1–10, doi:10.1016/j.epsl.2010.10.005.

Freed, A. M., G. Hirth, and M. D. Behn (2012), Using short-term postseismic displacements to infer the ambient deformation conditions of the upper mantle, *J. Geophys. Res.*, *117*, B01409, doi:10.1029/2011JB008562.

Ghimire, S., and Y. Tanioka (2011), Spatial distribution of stress and frictional strength along the interplate boundary in northern Japan and its correlation to the locations of large earthquakes, *Tectonophysics*, *511*, 1–13.

Hall, R., J. R. Ali, C. D. Anderson, and S. J. Baker (1995), Origin and motion history of the Philippine Sea Plate, *Tectonophysics*, *251*, 229–250.

Hashimoto, C., A. Noda, T. Sagiya, and M. Matsu'ura (2009), Interplate seismogenic zones along the Kuril–Japan trench inferred from GPS data inversion, *Nat. Geosci.*, *2*, 141–144, doi:10.1038/NGEO421.

Hayes, G. P., D. J. Wald, and R. L. Johnson (2012), Slab1.0: A three-dimensional model of global subduction zone geometries, *J. Geophys. Res.*, *117*, B01302, doi:10.1029/2011JB008524.

Hearn, E. H., R. Bürgmann, and R. E. Reilinger (2002), Dynamics of İzmit earthquake postseismic deformation and loading of the Düzce Earthquake Hypocenter, *Bull. Seismol. Soc. Am.*, *92*(1), 172–193.

Hearn, E. H., S. McClusky, S. Ergintav, and R. E. Reilinger (2009), Izmit earthquake postseismic deformation and dynamics of the North Anatolian Fault Zone, *J. Geophys. Res.*, *114*, B08405, doi:10.1029/2008JB006026.

Heki, K. (2004), Space geodetic observation of deep basal subduction erosion in the Northeastern Japan, *Earth Planet. Sci. Lett.*, *219*, 13–20.

Heki, K. (2007), Secular, transient and seasonal crustal movements in Japan from a dense GPS array: Implication for plate dynamics in convergent boundaries, in *The Seismogenic Zone of Subduction Thrust Faults*, edited by T. Dixon and C. Moore, pp. 512–539, Columbia Univ. Press, New York.

Hirose, H., and K. Obara (2006), Short-term slow slip and correlated tremor episodes in the Tokai region, central Japan, *Geophys. Res. Lett.*, *33*, L17311, doi:10.1029/2006GL026579.

Hoechner, A., S. V. Sobolev, I. Einarsson, and R. Wang (2011), Investigation on afterslip and steady state and transient rheology based on postseismic deformation and geoid change caused by the Sumatra 2004 earthquake, *Geochem. Geophys. Geosyst.*, *12*, Q07010, doi:10.1029/2010GC003450.

Hu, Y., and K. Wang (2012), Spherical-Earth finite element model of short-term postseismic deformation following the 2004 Sumatra earthquake, *J. Geophys. Res.*, *117*, B05404, doi:10.1029/2012JB009153.

Hu, Y., K. Wang, J. He, J. Klotz, and G. Khazaradze (2004), Three-dimensional viscoelastic finite element model for post-seismic deformation of the great 1960 Chile earthquake, *J. Geophys. Res.*, *109*, B12403, doi:10.1029/2004JB003163.
Hu, Y., R. Bürgmann, J. T. Freymueller, P. Banerjee, and K. Wang (2014), Contributions of poroelastic rebound and a weak volcanic arc to the postseismic deformation of the 2011 Tohoku earthquake, *Earth Planet Sci.*, *66*, 106, doi:10.1186/1880-5981-66-106.
Hughes, K. L. H., T. Masterlark, and W. D. Mooney (2010), Poroelastic stress-triggering of the 2005 *M*8.7 Nias earthquake by the 2004 *M*9.2 Sumatra–Andaman earthquake, *Earth Planet. Sci. Lett.*, *293*(3–4), 289–299, doi:10.1016/j.epsl.2010.02.043.
Igarashi, T., T. Matsuzawa, and A. Hasegawa (2003), Repeating earthquakes and interplate aseismic slip in the northeastern Japan subduction zone, *J. Geophys. Res.*, *108*(B5), 2249, doi:10.1029/2002JB001920.
Iinuma, T., et al. (2012), Coseismic slip distribution of the 2011 off the Pacific Coast of Tohoku Earthquake (*M*9.0) refined by means of seafloor geodetic data, *J. Geophys. Res.*, *117*, B07409, doi:10.1029/2012JB009186.
Japan Coast Guard (2012), Seafloor movements obtained by seafloor geodetic observations after the 2011 off the Pacific Coast of Tohoku earthquake, *Rep. Coord. Comm. Earthquake Predict.*, *88*, 150–154, (In Japanese).
Japan Coast Guard, and Tohoku University (2013), Seafloor movements observed by seafloor geodetic observations after the 2011 off the Pacific coast of Tohoku Earthquake, *Rep. Coord. Comm. Earthquake Predict. Jpn.*, *90*, 3–4.
Johnson, K. M., R. Bürgmann, and K. Larson (2006), Frictional on the San Andreas fault near Parkfield, California, inferred from models of afterslip following the 2004 earthquake, *Bull. Seismol. Soc. Am.*, *96*, 321–338, doi:10.1785/0120050808.
Johnson, K. M., J. Fukuda, and P. Segall (2012), Challenging the rate-state asperity model: Afterslip following the 2011 *M*9 Tohoku-oki, Japan, earthquake, *Geophys. Res. Lett.*, *39*, L20302, doi:10.1029/2012GL052901.
Jónsson, S., H. Zebker, P. Segall, and F. Amelung (2002), Fault slip distribution of the 1999 $M_w$ 7.1 Hector Mine, California, Earthquake, estimated from satellite radar and GPS measurements, *Bull. Seismol. Soc. Am.*, *92*(4), 1377–1389.
Kanamori, H. (2014), The diversity of large earthquakes and its implications for hazard mitigation, *Annu. Rev. Earth Planet. Sci.*, *42*, 7–26, doi:10.1146/annurev-earth-060313-055034.
Kato, A., and T. Igarashi (2012), Regional extent of the large coseismic slip zone of the 2011 $M_w$ 9.0 Tohoku-Oki earthquake delineated by on-fault aftershocks, *Geophys. Res. Lett.*, *39*, L15301, doi:10.1029/2012GL052220.
Kato, T. (1983), Secular and earthquake-related vertical crustal movements in Japan as deduced from tidal records (1951–1981), *Tectonophysics*, *97*, 183–200.
Kawakatsu, H., P. Kumar, Y. Takei, M. Shinohara, T. Kanazawa, E. Araki, and K. Suyehiro (2009), Seismic evidence for sharp lithosphere-asthenosphere boundaries of oceanic plates, *Science*, *324*, 499–502, doi:10.1126/science.1169499.
Kimura, G., and K. Tamaki (1986), Collision, rotation, and back-arc spreading in the region of the Okhotsk and Japan Seas, *Tectonics*, *5*, 389–401, doi:10.1029/TC005i003p00389.
Klotz, J., G. Khazaradze, D. Angermann, C. Reigber, R. Perdomo, and O. Cifuentes (2001), Earthquake cycle dominates contemporary crustal deformation in Central and Southern Andes, *Earth Planet. Sci. Lett.*, *193*, 437–446, doi:10.1016/S0012-821X(01)00532-5.
Koike, K., and H. Machida (2001), *Atlas of Marine Terraces of Japan*, 105 pp., Univ. of Tokyo Press, Tokyo.
Lay, T. (2014), The surge of great earthquakes from 2004 to 2014, *Earth Planet. Sci. Lett.*, *409*, 133–146, doi:10.1016/j.epsl.2014.10.047.
Li, C., and R. D. van der Hilst (2010), Structure of the upper mantle and transition zone beneath Southeast Asia from travel time tomography, *J. Geophys. Res.*, *115*, B07308, doi:10.1029/2009JB006882.
Lubis, A. M., A. Hashima, and T. Sato (2013), Analysis of afterslip distribution following the 2007 September 12 southern Sumatra earthquake using poroelastic and viscoelastic media, *Geophys. J. Int.*, *192*, 18–37, doi:10.1093/gji/ggs020.
Matsu'ura, T., A. Furusawa, and H. Saomoto (2009), Long-term and short-term vertical velocity profiles across the forearc in the NE Japan subduction zone, *Quat. Res.*, *71*, 227–238, doi:10.1016/j.yqres.2008.12.005.
Mavrommatis, A. P., P. Segall, and K. M. Johnson (2014), A decadal-scale deformation transient prior to the 2011 $M_w$ 9.0 Tohoku-Oki earthquake, *Geophys. Res. Lett.*, *41*, 4486–4494, doi:10.1002/2014GL060139.
McCaffrey, R., R. W. King, S. J. Payne, and M. Lancaster (2013), Active tectonics of northwestern U.S. inferred from GPS-derived surface velocities, *J. Geophys. Res. Solid Earth*, *118*, 709–723, doi:10.1029/2012JB009473.
Meade, B. J., Y. Klinger, and E. A. Hetland (2013), Inference of multiple earthquake-cycle relaxation timescales from irregular geodetic sampling of interseismic deformation, *Bull. Seismol. Soc. Am.*, *103*(5), 2824–2835, doi:10.1785/0120130006.
Melosh, H. J., and A. Raefsky (1981), A simple and efficient method for introducing faults into finite element computations, *Bull. Seismol. Soc. Am.*, *71*, 1391–1400.
Melosh, H. J., and A. Raefsky (1983), Anelastic response of the Earth to a dip slip earthquake, *J. Geophys. Res.*, *88*(B1), 515–526, doi:10.1029/JB088iB01p00515.
Mikhailov, V., V. Lyakhovsky, I. Panet, Y. van Dinther, M. Diament, T. Gerya, and E. Timoshkina (2013), Numerical modelling of post-seismic rupture propagation after the Sumatra 26.12.2004 earthquake constrained by GRACE gravity data, *Geophys. J. Int.*, *194*(2), 640–650, doi:10.1093/gji/ggt145.
Minoura, K., F. Imamura, D. Sugawara, Y. Kono, and T. Iwashita (2001), The 869 Jōgan tsunami deposit and recurrence interval of large-scale tsunami on the Pacific coast of northeast Japan, *J. Nat. Disaster Sci.*, *23*, 83–88.
Miyazaki, S., and Y. Hatanaka (1998), The outlines of the GEONET [in Japanese], *Meteorol. Res. Note*, *192*, 105–131.
Munekane, H. (2012), Coseismic and early postseismic slips associated with the 2011 off the Pacific coast of Tohoku earthquake sequence: EOF analysis of GPS kinematic time series, *Earth Planets Space*, *64*(12), 1077–1091.
Muto, J., B. Shibazaki, Y. Ito, T. Iinuma, M. Ohzono, T. Matsumoto, and T. Okada (2013), Two–dimensional viscosity structure of the northeastern Japan islands arc-trench system, *Geophys. Res. Lett.*, *40*, 4604–4608, doi:10.1002/grl.50906.
Nadeau, R. M., and L. R. Johnson (1998), Seismological studies at Parkfield VI: Moment release rates and estimates of source parameters for small repeating earthquakes, *Bull. Seismol. Soc. Am.*, *88*, 790–814.
Nakada, S., M. Nagai, T. Kaneko, A. Nozawa, and K. Suzuki-Kamata (2005), Chronology and products of the 2000 eruption of Miyakejima Volcano, Japan, *Bull. Volcanol.*, *67*, 205–218, doi:10.1007/s00445-004-0404-4.
Nakajima, J., and A. Hasegawa (2006), Anomalous low-velocity zone and linear alignment of seismicity along it in the subducted Pacific slab beneath Kanto, Japan: Reactivation of subducted fracture zone?, *Geophys. Res. Lett.*, *33*, L16309, doi:10.1029/2006GL026773.
Nishimura, T., M. Sato, and T. Sagiya (2014), Global Positioning System (GPS) and GPS-Acoustic observations: Insight into slip along the subduction zones around Japan, *Annu. Rev. Earth Planet. Sci.*, *42*, 653–674, doi:10.1146/annurev-earth-060313-054614.
Obayashi, M., J. Yoshimitsu, and Y. Fukao (2009), Tearing of stagnant slab, *Science*, *324*, 1173–1175, doi:10.1126/science.1172496.
Okada, Y. (1985), Surface deformation due to shear and tensile faults in a half-space, *Bull. Seismol. Soc. Am.*, *75*, 1135–1154.
Ota, Y., and M. Yamaguchi (2004), Holocene coastal uplift in the western Pacific Rimin the context of late Quaternary uplift, *Quat. Int.*, *120*, 105–117, doi:10.1016/j.quaint.2004.01.010.

Ozawa, S. (2014), Shortening of recurrence interval of Boso slow slip events in Japan, *Geophys. Res. Lett.*, *41*, 2762–2768, doi:10.1002/2014GL060072.
Ozawa, S., T. Nishimura, H. Munekane, H. Suito, T. Kobayashi, M. Tobita, and T. Imakiire (2012), Preceding, coseismic, and postseismic slips of the 2011 Tohoku earthquake, Japan, *J. Geophys. Res.*, *117*, B07404, doi:10.1029/2011JB009120.
Panet, I., F. Pollitz, V. Mikhailov, M. Diament, P. Banerjee, and K. Grijalva (2010), Upper mantle rheology from GRACE and GPS postseismic deformation after the 2004 Sumatra-Andaman earthquake, *Geochem. Geophys. Geosyst.*, *11*, Q06008, doi:10.1029/2009GC002905.
Peacock, S. M., and K. Wang (1999), Seismic consequences of warm versus cool subduction metamorphism: Examples from southwest and northeast Japan, *Science*, *286*, 937–939, doi:10.1126/science.286.5441.937.
Pollitz, F. F. (2003), Transient rheology of the uppermost mantle beneath the Mojave Desert, California, *Earth Planet. Sci. Lett.*, *215*, 89–104, doi:10.1016/S0012-821X(03)00432-1.
Pollitz, F. F. (2005), Transient rheology of the upper mantle beneath central Alaska inferred from the crustal velocity field following the 2002 Denali earthquake, *J. Geophys. Res.*, *110*, B08407, doi:10.1029/2005JB003672.
Pollitz, F. F., R. Bürgmann, and B. Romanowicz (1998), Viscosity of oceanic asthenosphere inferred from remote triggering of earthquakes, *Science*, *280*, 1245–1249.
Pollitz, F. F., R. Bürgmann, and P. Banerjee (2006), Post-seismic relaxation following the great 2004 Sumatra-Andaman earthquake on a compressible self-gravitating Earth, *Geophys. J. Int.*, *167*(1), 397–420, doi:10.1111/j.1365-1246X.2006.03018.x.
Pollitz, F. F., P. Banerjee, K. Grijalva, B. Nagarajan, and R. B. Bürgmann (2008), Effect of 3-D viscoelastic structure on post-seismic relaxation from the 2004 $M = 9.2$ Sumatra earthquake, *Geophys. J. Int.*, *173*(1), 189–204, doi:10.1111/j.1365-246X.2007.03666.x.
Rousset, B., S. Barbot, J.-P. Avouac, and Y.-J. Hsu (2012), Postseismic deformation following the 1999 Chi-Chi earthquake, Taiwan: Implication for lower-crust rheology, *J. Geophys. Res.*, *117*, B12405, doi:10.1029/2012JB009571.
Ruina, A. (1983), Slip instability and state variable friction laws, *J. Geophys. Res.*, *88*, 10,359–10,370, doi:10.1029/JB088iB12p10359.
Sabadini, R., D. A. Yuen, and P. Gasperini (1985), The effects of transient rheology on the interpretation of lower mantle viscosity, *Geophys. Res. Lett.*, *12*, 361–364, doi:10.1029/GL012i006p00361.
Sagiya, T. (2015), Paradoxical vertical crustal movement along the Pacific coast of Northeast Japan, in *International Associated of Geodesy Symposia*, pp. 1–6, Springer, Berlin, doi:10.1007/1345_2015_189.
Sato, K., T. Baba, T. Hori, M. Hyodo, and Y. Kaneda (2010), Afterslip distribution following the 2003 Tokachi-oki earthquake: An estimation based on the Green's functions for an inhomogeneous elastic space with subsurface structure, *Earth Planets Space*, *62*, 923–932, doi:10.5047/eps.2010.11.007.
Sato, M., M. Fujita, Y. Matsumoto, T. Ishikawa, H. Saito, M. Mochizuki, and A. Asada (2013), Interplate coupling off northeastern Japan before the 2011 Tohoku-Oki earthquake, inferred from seafloor geodetic data, *J. Geophys. Res. Solid Earth*, *118*, 3860–3869, doi:10.1002/jgrb.50275.
Savage, J. C. (1983), A dislocation model of strain accumulation and release at a subduction zone, *J. Geophys. Res.*, *88*, 4984–4996, doi:10.1029/JB088iB06p04984.
Sawai, Y., Y. Fujii, O. Fujiwara, T. Kamataki, J. Komatsubara, Y. Okamura, K. Satake, and M. Shishikura (2008), Marine incursions of the past 1500 years and evidence of tsunamis at Suijin-numa, a coastal lake facing the Japan Trench, *Holocene*, *18*(4), 517–528, doi:10.1177/0959683608089206.
Sawai, Y., Y. Namegaya, Y. Okamura, K. Satake, and M. Shishikura (2012), Challenges of anticipating the 2011 Tohoku earthquake and tsunami using coastal geology, *Geophys. Res. Lett.*, *39*, L21309, doi:10.1029/2012GL053692.
Spada, G. (2003), *The Theory Behind TABOO*, Samizdat Press, Golden - White River Junction, Italy.
Suito, H., and J. T. Freymueller (2009), A viscoelastic and afterslip postseismic deformation model for the 1964 Alaska earthquake, *J. Geophys. Res.*, *114*, B11404, doi:10.1029/2008JB005954.
Sun, T., et al. (2014), Prevalence of viscoelastic relaxation after the 2011 Tohoku-Oki earthquake, *Nature*, *514*, 84–87, doi:10.1038/nature13778.
Suwa, Y., S. Miura, A. Hasegawa, T. Sato, and K. Tachibana (2006), Interplate coupling beneath NE Japan inferred from three-dimensional displacement field, *J. Geophys. Res.*, *111*, B04402, doi:10.1029/2004JB003203.
Tomita, F., M. Kido, Y. Osada, R. Hino, Y. Ohta, and T. Iinuma (2015), First measurement of the displacement rate of the Pacific Plate near the Japan Trench after the 2011 Tohoku-Oki earthquake using GPS/acoustic technique, *Geophys. Res. Lett.*, *42*, 8391–8397, doi:10.1002/2015GL065746.
Toscano, M. A., W. R. Peltier, and R. Drummond (2011), ICE-5G and ICE-6G models of postglacial relative sea-level history applied to the Holocene coral reef record of northeastern St Croix, U.S.V.I.: Investigating the influence of rotational feedback on GIA processes at tropical latitudes, *Quat. Sci. Rev.*, *30*(21–22), 3032–3042, doi:10.1016/j.quascirev.2011.07.018.
Trubienko, O., J.-D. Garaud, and L. Fleitout (2014), Models of postseismic deformation after megaearthquakes: The role of various rheological and geometrical parameters of the subduction zone, *Solid Earth Discuss.*, *6*, 427–466, doi:10.5194/sed-6-427-2014.
Uchida, N., and T. Matsuzawa (2013), Pre-and postseismic slow slip surrounding the 2011 Tohoku-Oki earthquake rupture, *Earth Planet. Sci. Lett.*, *374*, 81–91, doi:10.1016/j.epsl.2013.05.021.
Uchida, N., S. H. Kirby, T. Okada, R. Hino, and A. Hasegawa (2010a), Supraslab earthquake clusters above the subduction plate boundary offshore Sanriku, northeastern Japan: Seismogenesis in a graveyard of detached seamounts?, *J. Geophys. Res.*, *115*, B09308, doi:10.1029/2009JB006797.
Uchida, N., T. Matsuzawa, J. Nakajima, and A. Hasegawa (2010b), Subduction of a wedge-shaped Philippine Sea plate beneath Kanto, central Japan, estimated from converted waves and small repeating earthquakes, *J. Geophys. Res.*, *115*, B07309, doi:10.1029/2009JB006962.
von Huene, R., D. Klaeschen, B. Cropp, and J. Miller (1994), Tectonic structure across the accretionary and erosional parts of the Japan trench margin, *J. Geophys. Res.*, *99*, 22,349–22,361, doi:10.1029/94JB01198.
von Huene, R., C. R. Ranero, and P. Vannucchi (2004), Generic model of subduction erosion, *Geology*, *32*(10), 913–916, doi:10.1130/G20563.1.
Wada, I., and K. Wang (2009), Common depth of slab-mantle decoupling: Reconciling diversity and uniformity of subduction zones, *Geochem. Geophys. Geosyst.*, *10*, Q10009, doi:10.1029/2009GC002570.
Wang, K. (2007), Elastic and viscoelastic models of subduction earthquake cycles, in *The Seismogenic Zone of Subduction Thrust Faults*, edited by T. H. Dixon and J. C. Moore, pp. 540–575, Columbia Univ. Press, New York.
Wang, K., R. E. Wells, S. Mazzotti, R. D. Hyndman, and T. Sagiya (2003), A revised dislocation model of interseismic deformation of the Cascadia subduction zone, *J. Geophys. Res.*, *108*(B1), 2026, doi:10.1029/2001JB001227.
Wang, K., Y. Hu, M. Bevis, E. Kendrick, R. Smalley Jr., R. B. Vargas, and E. Lauría (2007), Crustal motion in the zone of the 1960 Chile earthquake: Detangling earthquake-cycle deformation and forearc-sliver translation, *Geochem. Geophys. Geosyst.*, *8*, Q10010, doi:10.1029/2007GC001721.
Wang, K., Y. Hu, and J. He (2012), Deformation cycles of subduction earthquakes in a viscoelastic Earth, *Nature*, *484*, 327–332, doi:10.1038/nature11032.

Wang, R., F. Lorenzo-Martín, and F. Roth (2003), Computation of deformation induced by earthquakes in a multi-layered elastic crust—FORTRAN programs EDGRN/EDCMP, *Comput. Geosci.*, *29*(2), 195–207.

Watanabe, S., M. Sato, M. Fujita, T. Ishikawa, Y. Yokota, N. Ujihara, and A. Asada (2014), Evidence of viscoelastic deformation following the 2011 Tohoku-Oki earthquake revealed from seafloor geodetic observation, *Geophys. Res. Lett.*, *41*, 5789–5796, doi:10.1002/2014GL061134.

Wei, S., D. Helmberger, and J.-P. Avouac (2013), Modeling the 2012 Wharton basin earthquakes off-Sumatra: Complete lithospheric failure, *J. Geophys. Res. Solid Earth*, *118*, 3592–3609, doi:10.1002/jgrb.50267.

Weldon, R., K. Scharer, T. Fumal, and G. Biasi (2004), Wrightwood and the earthquake cycle: What a long recurrence record tells us about how faults work, *GSA Today*, *14*(9), 4–10.

Welstead, S. T. (1999), *Fractal and Wavelet Image Compression Techniques*, 232 pp., SPIE Opt. Eng. Press, Bellingham, Wash.

Wiseman, K., R. Bürgmann, A. M. Freed, and P. Banerjee (2015), Viscoelastic relaxation in a heterogeneous Earth following the 2004 Sumatra-Andaman earthquake, *Earth Planet. Sci. Lett.*, *431*, 308–317, doi:10.1016/j.epsl.2015.09.024.

Yamagiwa, S., S. Miyazaki, K. Hirahara, and Y. Fukahata (2015), Afterslip and viscoelastic relaxation following the 2011 Tohoku-Oki earthquake ($M_w$9.0) inferred from inland GPS and seafloor GPS/Acoustic data, *Geophys. Res. Lett.*, *42*, 66–73, doi:10.1002/2014GL061735.

Yamanaka, Y., and M. Kikuchi (2004), Asperity map along the subduction zone in northeastern Japan inferred from regional seismic data, *J. Geophys. Res.*, *109*, B07307, doi:10.1029/2003JB002683.

Zhao, D., T. Matsuzawa, and A. Hasegawa (1997), Morphology of the subducting slab boundary in the northeastern Japan arc, *Phys. Earth Planet. Inter.*, *102*, 89–104, doi:10.1016/S0031-9201(96)03258-X.

Zhao, D., Z. Wang, N. Umino, and A. Hasegawa (2009), Mapping the mantle wedge and interplate thrust zone of the northeast Japan arc, *Tectonophysics*, *467*, 89–106, doi:10.1016/j.tecto.2008.12.017.